
Computational Advantages of Multi-Grade Deep Learning: Convergence Analysis and Performance Insights

Ronglong Fang, Yuesheng Xu

Department of Mathematics and Statistics, Old Dominion University
{rfang002, y1xu}@odu.edu

Abstract

Multi-grade deep learning (MGDL) has been shown to significantly outperform the standard single-grade deep learning (SGDL) across various applications. This work aims to investigate the computational advantages of MGDL focusing on its performance in image regression, denoising, and deblurring tasks, and comparing it to SGDL. We establish convergence results for the gradient descent (GD) method applied to these models and provide mathematical insights into MGDL's improved performance. In particular, we demonstrate that MGDL is more robust to the choice of learning rate under GD than SGDL. Furthermore, we analyze the eigenvalue distributions of the Jacobian matrices associated with the iterative schemes arising from the GD iterations, offering an explanation for MGDL's enhanced training stability. The code used to generate the numerical results is available on GitHub: Computational Advantages of MGDL.

1 Introduction

Deep learning has achieved remarkable success across various domains, fundamentally transforming computer vision, natural language processing, speech recognition, medicine, and scientific computing. In computer vision, deep convolutional neural networks (CNNs) have driven major breakthroughs in image recognition and classification [12, 18, 32]. In natural language processing, transformer-based architectures [33] have revolutionized tasks such as machine translation, chatbots, and sophisticated text generation. Speech recognition has advanced significantly through recurrent neural networks (RNNs) and long short-term memory (LSTM) networks [13, 31], enabling end-to-end learning from raw audio signals. Beyond these traditional domains, deep learning has profoundly impacted scientific computing, accelerating discoveries in physics, chemistry, biology, and medicine. Notable applications include protein structure prediction [15], drug discovery [4], and solving complex partial differential equations [27]. These achievements highlight deep learning's transformative role across both theoretical and applied sciences.

Despite its success—driven by advances in neural network architectures, optimization techniques, and computational power—deep learning continues to face significant challenges in explainability, efficiency, and generalization. Training a deep neural network (DNN) involves solving a highly non-convex optimization problem, complicated by the large number of layers and parameters. Optimization algorithms often become trapped in local minima, and iterative training methods suffer from vanishing or exploding gradients due to the repeated application of the chain rule. Additionally, DNNs exhibit spectral bias [26, 39], prioritizing low-frequency components during training, which can limit their ability to capture fine details. Moreover, the analysis in [5] shows that during gradient descent (GD), the maximum eigenvalue of the Hessian tends to hover just above $2/(\text{learning rate})$, contributing to training instability. Current training paradigms largely operate as black boxes, lacking interpretability, computational efficiency, and robust generalization.

To address these challenges, Xu [37] recently introduced multi-grade deep learning (MGDL), inspired by human learning systems. Instead of optimizing the loss function end-to-end, MGDL decomposes the learning process into a sequence of smaller optimization problems, each training a shallow neural network with only a few hidden layers. These problems are structured into multiple grades, where each grade learns from the residuals of the previous one. At each stage, a new shallow network is trained while being composed with previously learned networks, whose parameters remain fixed and serve as features or adaptive ‘basis’ functions. This iterative refinement process progressively enhances learning while significantly reducing the complexity of the optimization problem.

MGDL has been shown to significantly outperform standard single-grade deep learning (SGDL) in applications such as regression [7, 36], numerical solutions of oscillatory Fredholm integral equations [14], and numerical solutions of partial differential equations [38]. Notably, MGDL effectively mitigates spectral bias [26, 39]. For a general numerical study of this phenomenon, see [7]; its effectiveness in solving oscillatory Fredholm integral equations is demonstrated in [14], while [37] applies MGDL to solving the Helmholtz equation. The goal of this paper is to investigate why MGDL outperforms SGDL by analyzing the computational advantages it offers. Since most optimization algorithms used in training deep neural networks (DNNs) are modifications of the GD method, we focus on studying GD applied to the optimization problems arising in both MGDL and SGDL. Specifically, we establish convergence theorems for GD in the MGDL framework and, based on these results, demonstrate that MGDL exhibits greater robustness to the learning rate compared to SGDL.

To analyze the convergence of MGDL and SGDL, we study a linear surrogate iterative scheme defined by the Jacobian matrix of the nonlinear map associated with the original iterative scheme. We show that the sequence generated by this surrogate scheme converges to the same limit as the sequence produced by the original scheme. Furthermore, we examine the eigenvalue distribution of the Jacobian matrices for the linear surrogate iterative schemes of MGDL and SGDL. Our numerical analysis reveals that the eigenvalues associated with MGDL are confined within the open interval $(-1, 1)$, whereas those for SGDL may extend beyond this range. This confirms that, in the cases studied, the GD method for MGDL converges, whereas for SGDL, it does not. This explains why the loss values for SGDL exhibit oscillations, while those for MGDL are significantly more stable.

The Multi-scale Deep Neural Network (MSDL) was introduced in [21, 34] to mitigate the issue of spectral bias in deep learning. MSDL consists of multiple parallel standard sub-networks, each operating on a scaled version of the input. The outputs of these sub-networks are then combined to produce the final prediction. Numerical experiments reports in these studies demonstrate that MSDL converges rapidly across a range of applications, including regression problems, Poisson–Boltzmann equations, and oscillatory Stokes flows. We conduct a numerical analysis of gradient descent applied to MSDL and compare its convergence behavior with that of MGDL. The analysis reveals that the eigenvalues of the iteration matrices associated with MSDL may lie outside the interval $(-1, 1)$, potentially leading to unstable training dynamics. This observation provides a theoretical explanation for the highly oscillatory loss function values reported in the numerical experiments of [21].

The key contributions of this paper are as follows:

- (a) We provide a rigorous convergence analysis of the GD method for SGDL and MGDL, demonstrating the computational advantages of MGDL in solving the corresponding optimization problems.
- (b) We conduct extensive numerical experiments, including image regression, denoising, and deblurring, showing that MGDL consistently outperforms SGDL and exhibits greater stability.
- (c) We study the impact of learning rate on SGDL and MGDL, showing that MGDL is more robust.
- (d) We analyze a linear approximation of the GD dynamics to explain the convergence behavior of SGDL and MGDL. Furthermore, we numerically verify the superior stability of MGDL by studying the eigenvalue distribution of the associated Jacobian matrix.

2 Standard Deep Learning Model

In this section, we review the standard deep learning model and analyze the convergence behavior of the gradient descent (GD) method when applied to the resulting optimization problem.

We begin with a quick review of the definition of DNNs. A DNN is a composition of affine transformations and activation functions, consisting of an input layer, $D - 1$ hidden layers, and an

output layer. Let $d_0 := d$ (input dimension) and $d_D := s$ (output dimension), and denote the number of neurons in the j -th layer by d_j . For $j \in \mathbb{N}_D := \{1, 2, \dots, D\}$, the weight matrices and bias vectors are $\mathbf{W}_j \in \mathbb{R}^{d_{j-1} \times d_j}$ and $\mathbf{b}_j \in \mathbb{R}^{d_j}$, respectively. The activation function $\sigma: \mathbb{R} \rightarrow \mathbb{R}$, applied componentwise, is taken to be ReLU: $\sigma(x) = (x)_+ := \max\{0, x\}$.

Given an input $\mathbf{x} \in \mathbb{R}^d$, the hidden layers are defined recursively by

$$\mathcal{H}_1(\mathbf{x}) := \sigma(\mathbf{W}_1^\top \mathbf{x} + \mathbf{b}_1), \mathcal{H}_{j+1}(\mathbf{x}) := \sigma(\mathbf{W}_{j+1}^\top \mathcal{H}_j(\mathbf{x}) + \mathbf{b}_{j+1}), j = 1, \dots, D-2.$$

The network output is then given by $\mathcal{N}_D(\{\mathbf{W}_j, \mathbf{b}_j\}_{j=1}^D; \mathbf{x}) = \mathcal{N}_D(\mathbf{x}) := \mathbf{W}_D^\top \mathcal{H}_{D-1}(\mathbf{x}) + \mathbf{b}_D$. For a dataset $\mathbb{D} := \{\mathbf{x}_\ell, \mathbf{y}_\ell\}_{\ell=1}^N$, the loss function is

$$\mathcal{L}(\{\mathbf{W}_j, \mathbf{b}_j\}_{j=1}^D; \mathbb{D}) := \frac{1}{2N} \sum_{\ell=1}^N \|\mathbf{y}_\ell - \mathcal{N}_D(\{\mathbf{W}_j, \mathbf{b}_j\}_{j=1}^D; \mathbf{x}_\ell)\|^2. \quad (1)$$

The standard SGDL model minimizes this loss with respect to the network parameter $\Theta := \{\mathbf{W}_j, \mathbf{b}_j\}_{j=1}^D$, yielding the optimal parameters Θ^* and the trained network $\mathcal{N}_D(\Theta^*, \cdot)$.

Among commonly used methods for solving optimization problems for deep learning are stochastic gradient descent (SGD) [16, 28] and adaptive moment estimation (Adam) [17]. Most of them are based on GD. For this reason, we will study GD for minimizing the loss function defined in (1). To facilitate the convergence analysis, we stack all network parameters $\{\mathbf{W}_j, \mathbf{b}_j\}_{j=1}^D$ into a single column vector. For this purpose, we introduce the following notation. Given a matrix or vector \mathbf{A} , we denote its vectorization by A : If \mathbf{A} is a matrix, A is the column vector obtained by stacking the columns of \mathbf{A} . If \mathbf{A} is already a column vector, then $A = \mathbf{A}$. If \mathbf{A} is a row vector, then $A = \mathbf{A}^\top$. We define the parameter vector $W := (W_1^\top, b_1^\top, \dots, W_D^\top, b_D^\top)^\top$, where the total number of parameters is $M := \sum_{j=1}^D (d_{j-1} + 1)d_j$. We consider GD applied to a general objective function $\mathcal{F}: \mathbb{R}^M \rightarrow \mathbb{R}$, assumed to be nonnegative, twice continuously differentiable, and generally nonconvex. The GD iteration is given by

$$W^{k+1} := W^k - \eta \frac{\partial \mathcal{F}}{\partial W}(W^k), \quad (2)$$

where k denotes the iteration index and $\eta > 0$ is the learning rate. In the context of this paper, we are particularly interested in the case where \mathcal{F} is the loss function \mathcal{L} defined in (1).

We now analyze the convergence of the GD method for minimizing the loss function (1). Assume there exists a compact, convex set $\mathcal{W} \subset \mathbb{R}^M$ such that for all $\eta \in (0, \eta_0)$ (for some $\eta_0 > 0$), the GD iterates $\{W^k\}_{k=0}^\infty$ from (2) with $\mathcal{F} := \mathcal{L}$ remain in \mathcal{W} . Convergence depends on the Hessian of \mathcal{L} over \mathcal{W} , for which we define $\alpha := \sup_{W \in \mathcal{W}} \|\mathbf{H}_{\mathcal{L}}(W)\|$, where $\|\cdot\|$ denotes the spectral norm. Since $\mathbf{H}_{\mathcal{L}}(W) \in \mathbb{R}^{M \times M}$, the constant α reflects the network's depth and size. The following theorem, proved in Appendix B, establishes the convergence of GD with $\mathcal{F} := \mathcal{L}$, extending the approach of Theorem 6 in [37], which assumes all biases are zero.

Theorem 1. *Let $\{W^k\}_{k=1}^\infty$ be a sequence generated by the gradient descent iteration (2) with $\mathcal{F} := \mathcal{L}$ and initial guess W^0 . Suppose the activation function σ is twice continuously differentiable, and there exists a convex compact set $\mathcal{W} \subset \mathbb{R}^M$ such that $\{W^k\}_{k=1}^\infty \subset \mathcal{W}$. If the learning rate $\eta \in (0, 2/\alpha)$, then the following statements hold:*

- (i) $\lim_{k \rightarrow \infty} \mathcal{L}(W^k) = L^*$ for some $L^* \geq 0$;
- (ii) $\lim_{k \rightarrow \infty} \frac{\partial \mathcal{L}}{\partial W}(W^k) = 0$;
- (iii) Every cluster point \hat{W} of $\{W^k\}_{k=0}^\infty$ satisfies $\frac{\partial \mathcal{L}}{\partial W}(\hat{W}) = 0$.

Deep neural networks are characterized by weight matrices and bias vectors, with parameter counts growing rapidly with depth—for instance, LeNet-5 [19] has 60K parameters, ResNet-152 [12] 60.2M, and GPT-3 [3] 175B. Traditional end-to-end training becomes increasingly difficult at scale due to both optimization and stability issues. First, deeper networks lead to highly nonconvex loss landscapes, often trapping solutions in poor local minima [2]. Second, training instability arises from vanishing or exploding gradients, which can hinder convergence [9, 10, 24]. To address these challenges, the multi-grade deep learning (MGDL) model [37] mimics the human education system, where learning progresses in stages. MGDL sequentially trains shallow networks, each building on and refining the output of the previous grade to incrementally approximate the target function.

3 Multi-Grade Deep Learning

This section reviews MGDL, analyzes GD convergence at each grade, and presents a convex program when each grade is a two-layer ReLU network.

Given data $\mathbb{D} := \{\mathbf{x}_\ell, \mathbf{y}_\ell\}_{\ell=1}^N$, MGDL [37] decomposes learning a DNN of depth D into $L < D$ sequential grades, each training a shallow neural network (SNN) \mathcal{N}_{D_l} on the residuals from the previous grade. The depths satisfy $1 < D_l < D$ and $\sum_{l=1}^L D_l = D + L - 1$. Let $\Theta_l := \{\mathbf{W}_{lj}, \mathbf{b}_{lj}\}_{j=1}^{D_l}$ be the parameters in grade l . The model is recursively defined by

$$g_l(\Theta_l; \mathbf{x}) := \mathcal{N}_{D_l}(\Theta_l; \mathbf{x}), \quad g_{l+1}(\Theta_{l+1}; \mathbf{x}) := \mathcal{N}_{D_{l+1}}(\Theta_{l+1}; \cdot) \circ \mathcal{H}_{D_{l-1}}(\Theta_l^*; \cdot) \circ \dots \circ \mathcal{H}_{D_1}(\Theta_1^*; \cdot)(\mathbf{x})$$

for $l \in \mathbb{N}_{L-1}$, with loss function $\mathcal{L}_l(\Theta_l; \mathbb{D}) := \frac{1}{2N} \sum_{\ell=1}^N \|\mathbf{e}_{l\ell} - g_l(\Theta_l; \mathbf{x}_\ell)\|^2$ where $\mathbf{e}_{1\ell} := \mathbf{y}_\ell$ and $\mathbf{e}_{(l+1)\ell} := \mathbf{e}_{l\ell} - g_l(\Theta_l^*; \mathbf{x}_\ell)$. Each Θ_l^* is obtained by minimizing \mathcal{L}_l while fixing previous parameters $\{\Theta_j^*\}_{j=1}^{l-1}$, which act as feature extractors. After training all L grades, the final MGDL output is the additive composition $\bar{g}_L(\{\Theta_l^*\}_{l=1}^L; \mathbf{x}) := \sum_{l=1}^L g_l(\Theta_l^*; \mathbf{x})$.

We apply the GD method to optimize each grade in MGDL. For clarity, define $\mathbf{x}_{1\ell} := \mathbf{x}_\ell$, and for $l = 2, \dots, L$ and $\ell = 1, \dots, N$, let $\mathbf{x}_{l\ell} := \mathcal{H}_{D_{l-1-1}}(\Theta_{l-1}^*; \cdot) \circ \dots \circ \mathcal{H}_{D_1}(\Theta_1^*; \cdot)(\mathbf{x}_\ell)$ and $\mathbb{D}_l := \{\mathbf{x}_{l\ell}, \mathbf{e}_{l\ell}\}_{\ell=1}^N$. The loss function $\mathcal{L}_l(\Theta_l; \mathbb{D})$ at grade l becomes

$$\mathcal{L}_l(\Theta_l; \mathbb{D}_l) := \frac{1}{2N} \sum_{\ell=1}^N \|\mathbf{e}_{l\ell} - \mathcal{N}_{D_l}(\Theta_l; \mathbf{x}_{l\ell})\|_2^2. \quad (3)$$

Each grade thus corresponds to a traditional shallow neural network whose input is the feature $\mathbf{x}_{l\ell}$ from previous grades and whose output approximates the residual. We apply GD (2) to minimize \mathcal{L}_l .

For grade l , define the parameter vector $W_l := (W_{l1}^\top, b_{l1}^\top, \dots, W_{lD_l}^\top, b_{lD_l}^\top)^\top \in \mathbb{R}^{M_l}$, where $M_l := \sum_{j=1}^{D_l} (d_{l(j-1)} + 1)d_{lj}$. The GD iteration is

$$W_l^{k+1} := W_l^k - \eta_l \frac{\partial \mathcal{L}_l}{\partial W_l}(W_l^k). \quad (4)$$

This is a special case of (2) with $\mathcal{F} := \mathcal{L}_l$ and $W := W_l$. Let $\mathcal{W}_l \subset \mathbb{R}^{M_l}$ be a convex compact set containing the GD iterates, and define $\alpha_l := \sup_{W_l \in \mathcal{W}_l} \|\mathbf{H}_{\mathcal{L}_l}(W_l)\|$. The following theorem proves convergence of the GD method (4) for grade l of MGDL. The proof is in Appendix B.

Theorem 2. *Let $\{W_l^k\}_{k=1}^\infty$ be the sequence generated by (4) from an initial guess W_l^0 . Assume the dataset $\{\mathbf{x}_{l\ell}, \mathbf{e}_{l\ell}\}_{\ell=1}^N \subset \mathbb{R}^{d_{l0}} \times \mathbb{R}^d$ is bounded. Suppose the activation function σ is twice continuously differentiable, and there exists a convex compact set $\mathcal{W}_l \subset \mathbb{R}^{M_l}$ such that $\{W_l^k\}_{k=1}^\infty \subset \mathcal{W}_l$. If the learning rate η_l is chosen from the interval $(0, 2/\alpha_l)$, then*

- (i) $\lim_{k \rightarrow \infty} \mathcal{L}_l(W_l^k) = L_l^*$ for some $L_l^* \geq 0$;
- (ii) $\lim_{k \rightarrow \infty} \frac{\partial \mathcal{L}_l}{\partial W_l}(W_l^k) = 0$;
- (iii) $\frac{\partial \mathcal{L}_l}{\partial W_l}(\hat{W}_l) = 0$ for any cluster point \hat{W}_l of $\{W_l^k\}_{k=0}^\infty$.

Theorem 1 parallels Theorem 2, with the main differences arising from the network depth. SGDL requires deep networks for expressiveness, while MGDL solves only a shallow network at each grade. This difference affects both the gradient behavior and the learning rate, which in turn influence the stability and performance of gradient descent. The gradient $\frac{\partial \mathcal{L}}{\partial W}$, as detailed in the Appendix of [37] and the Supplementary Material, involves a chain of D matrix products for depth- D networks. For large D , this can lead to vanishing or exploding gradients, degrading convergence and stability. MGDL mitigates this by restricting optimization to shallow networks, reducing such risks. Additionally, the allowable learning rate depends on the Hessian norm: SGDL requires $\eta \in (0, 2/\alpha)$, with α tied to a high-dimensional Hessian due to deep architecture. In contrast, MGDL only requires $\eta_l \in (0, 2/\alpha_l)$, where α_l is derived from a much smaller shallow network. Since $\alpha_l \ll \alpha$, MGDL supports a broader range of learning rates, enhancing robustness and training stability.

To close this section, we establish that when each grade of MGDL consists of one hidden layer ReLU network, the overall nonconvex optimization problem is reduced to solving a sequence of convex programming problems. It was shown in [6, 25] that training two-layer ReLU networks can be exactly

represented by a single convex program with the number of variables polynomial in the number of training samples and hidden neurons. Using this observation, MGDL with L grades transforms a highly nonconvex problem into L convex programs. We formulate the nonconvex problem for grade l as (8) and its corresponding convex program as (9) in Appendix A. The following theorem establishes their relationship. Since each grade of MGDL is essentially a two-layer ReLU network, the proof of the theorem follows directly from [25].

Theorem 3. *The convex program (9) and the non-convex problem (8) with $m_l \geq m_l^*$ have identical optimal values. Moreover, an optimal solution to (8) with $m_l^* := \sum_{i=1}^{P_l} (1[\mathbf{u}_{li}^* \neq 0] + 1[\mathbf{v}_{li}^* \neq 0])$ neurons can be constructed from an optimal solution to (9) as follows*

$$\begin{aligned} (\mathbf{w}_{lj_{1i}}^*, \alpha_{lj_{1i}}^*) &= \left(\frac{\mathbf{u}_{li}^*}{\sqrt{\|\mathbf{u}_{li}^*\|}}, \sqrt{\|\mathbf{u}_{li}^*\|} \right) \quad \text{if } \mathbf{u}_{li}^* \neq 0 \\ (\mathbf{w}_{lj_{2i}}^*, \alpha_{lj_{2i}}^*) &= \left(\frac{\mathbf{v}_{li}^*}{\sqrt{\|\mathbf{v}_{li}^*\|}}, -\sqrt{\|\mathbf{v}_{li}^*\|} \right) \quad \text{if } \mathbf{v}_{li}^* \neq 0, \end{aligned}$$

where $\{\mathbf{u}_{li}^*, \mathbf{v}_{li}^*\}_{i=1}^{P_l}$ are the optimal solutions to (9).

4 Comparison of SGDL and MGDL for Image Reconstruction

In this section, we apply SGDL and MGDL to image reconstruction tasks, including regression, denoising, and deblurring. Using the ReLU activation and PSNR (34) as the evaluation metric, we show that SGDL suffers from training instability and yields lower reconstruction accuracy than MGDL. TrPSNR and TePSNR denote PSNR values on the training and testing sets, respectively.

Image regression. We model grayscale images as 2D functions $f : \mathbb{R}^2 \rightarrow \mathbb{R}$, from pixel coordinates to intensity values. The training set comprises a regularly spaced grid covering 1/4 of the pixels, while the test set includes all pixels. We apply SGDL and MGDL to six images of various sizes (Figure 4). For images (b)–(f), we use structures (28) and (32); for image (g), we use (29) and (33).

We analyze the results for the ‘Cameraman’ image separately, as SGDL behaves differently for this image. The loss for SGDL and MGDL are shown in Figures 5 (a) and (b). SGDL exhibits extreme oscillations, leading to unstable predictions, as seen in Figures (c)–(f) for iterations 9800, 9850, 9900, and 9950, with oscillating PSNR. In contrast, the MGDL loss function steadily decreases (b), and its predictions (g)–(j) show consistent improvement, reflecting stable performance across iterations.

Numerical results for images (b)–(g) in Figure 4 are presented in Table 1 and Figure 6. Table 1 compares the PSNR values from SGDL and MGDL. MGDL outperforms SGDL by 0.42 to 3.94 dB in testing PSNR, with improvements for all images. Figure 6 shows the loss function for both methods. SGDL shows consistent oscillations across all images, while MGDL’s behavior varies. For images like Barbara, Butterfly, and Walnut, MGDL oscillates initially but stabilizes in later stages. For Pirate and Chest, MGDL oscillates more in earlier stages before stabilizing. These results suggest MGDL stabilizes or steadily decreases over time, while SGDL maintains persistent oscillations.

Table 1: PSNR comparison for image regression.

Image	Method	TrPSNR	TePSNR
Cameraman	SGDL	27.05	24.79
	MGDL	31.80	25.21
Barbara	SGDL	23.14	22.75
	MGDL	24.36	23.84
Butterfly	SGDL	26.22	24.87
	MGDL	28.23	27.06
Pirate	SGDL	24.20	24.34
	MGDL	27.40	26.45
Chest	SGDL	34.77	34.56
	MGDL	39.44	38.50
Walnut	SGDL	19.94	20.05
	MGDL	21.83	21.31

Table 2: PSNR comparison for image denoising.

Noise	Method	Butterfly	Pirate	Chest
10	SGDL	27.53	25.13	36.20
	MGDL	31.67	29.36	38.58
20	SGDL	26.73	25.02	35.34
	MGDL	28.39	27.74	36.89
30	SGDL	26.05	24.63	34.30
	MGDL	27.09	27.20	35.48
40	SGDL	25.54	24.47	33.55
	MGDL	26.37	26.25	34.61
50	SGDL	24.65	24.01	33.51
	MGDL	25.84	25.77	33.94
60	SGDL	24.30	23.82	32.90
	MGDL	25.21	25.32	33.06

Image denoising. We consider the image denoising problem. For a given noisy image $\hat{\mathbf{f}} := \mathbf{f} + \epsilon$ where $\hat{\mathbf{f}} \in \mathbb{R}^{n \times n}$ is the observed image, $\mathbf{f} \in \mathbb{R}^{n \times n}$ is the ground truth image, and $[\epsilon]_{i,j} \sim \mathcal{N}(0, \sigma^2)$

is the Gaussian noise with mean 0 and standard deviation σ . The task is to use SGDL and MGDL to recover the ground truth image \mathbf{f} from the observed noisy image $\hat{\mathbf{f}}$. The optimization problem is provided in Appendix C with the transform operator \mathbf{A} chosen as the identity operator.

The structures of SGDL and MGDL are given by (29) and (33), respectively. We test the models under six noise levels: $\sigma = 10, 20, 30, 40, 50, 60$, as shown in Figure 7. The results for image denoising are reported in Table 2 and Figures 8-10. Table 2 compares the PSNR values achieved by SGDL and MGDL across various images and noise levels. MGDL consistently outperforms SGDL, with improvements ranging from 0.16 to 4.23 dB in PSNR values. Figures 8-10 display the PSNR values during training. Across all cases, the PSNR values for SGDL exhibit strong oscillations throughout the training process, while those for MGDL increase steadily—especially for grades 2 to 4.

Image deblurring. We address the image deblurring problem, where the blurred image is modeled as $\hat{\mathbf{f}} := \mathbf{K}\mathbf{f} + \epsilon$, with $\hat{\mathbf{f}}$ as the observed image, \mathbf{K} as the Gaussian blurring operator, \mathbf{f} as the ground truth image, and $[\epsilon]_{i,j} \sim \mathcal{N}(0, \sigma^2)$ with $\sigma = 3$. The task is to recover \mathbf{f} from $\hat{\mathbf{f}}$ using SGDL and MGDL. The optimization problem and operator \mathbf{A} (Gaussian blurring operator) are detailed in Appendix C.

The structures of SGDL and MGDL are given by (29) and (33), respectively. We test the models under three blurring levels: $\hat{\sigma} = 3, \hat{\sigma} = 5$, and $\hat{\sigma} = 7$, as shown in Figure 11. Results, including PSNR values, are reported in Table 3 and Figures 12-14. MGDL outperforms SGDL by 0.85 to 2.84 dB in PSNR. While SGDL shows strong oscillations in PSNR during training, MGDL shows steady improvement, particularly from grades 2 to 4.

Table 3: PSNR comparison for image deblurring.

image	method	3	5	7
Butterfly	SGDL	25.43	24.20	22.70
	MGDL	27.06	25.19	23.65
Pirate	SGDL	24.72	23.79	23.13
	MGDL	26.47	24.95	23.98
Chest	SGDL	35.40	34.61	33.69
	MGDL	38.24	36.51	35.14

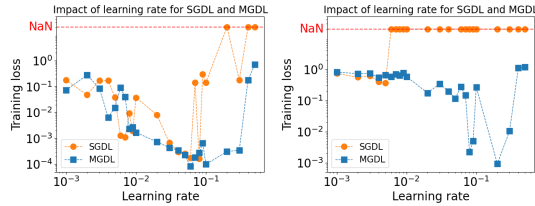


Figure 1: Impact of learning rate.

Results on image regression, denoising, and deblurring show that MGDL consistently outperforms SGDL. While SGDL exhibits strong oscillations in loss or PSNR during training, MGDL shows a steady decrease in loss or an increase in PSNR. The reasons for this will be explored in Section 6.

5 Impact of Learning Rate on SGDL and MGDL

This section explores the effect of learning rate on SGDL and MGDL. Both models are optimized by using the GD method. We evaluate various learning rates for both models to assess their performance.

Synthetic data regression. We approximate function $g : [0, 1] \rightarrow \mathbb{R}$ defined by

$$g(\mathbf{x}) := \sum_{j=1}^M \sin(2\pi\kappa_j\mathbf{x} + \varphi_j), \mathbf{x} \in [0, 1], \quad (5)$$

where $\varphi_j \sim \mathcal{U}(0, 2\pi)$, and \mathcal{U} denotes the uniform distribution. We consider two settings: (1) $M = 3, \kappa = [1, 5, 5, 10]$; (2) $M = 5, \kappa = [1, 8.25, 15.5, 22.75, 30]$. The training set contains 1024 equally spaced points in $[0, 1]$, and validation set contains 1000 points sampled uniformly from $[0, 1]$.

The structures of SGDL and MGDL follow (26) and (30), respectively. For both models, the learning rate is selected from the interval $[0.001, 0.5]$, with training run for 1×10^6 epochs. The impact of the learning rate on performance is illustrated in Figure 1 (left: Setting 1, right: Setting 2). In the figure, ‘NaN’ indicates that the training loss diverged, resulting in an invalid value. In Setting 1, where the target function has a lower frequency and is easier to approximate, both SGDL and MGDL perform well. However, MGDL is robust across a wider range of learning rates. Specifically, SGDL achieves a loss below 0.001 when the learning rate η lies in $[0.03, 0.08]$, whereas MGDL maintains this performance over a broader interval of $[0.01, 0.3]$. SGDL fails to converge when $\eta > 0.3$. In Setting 2, involving a higher-frequency target function, SGDL struggles with convergence for $\eta > 0.006$ and performs best at $\eta = 0.005$. By contrast, MGDL remains stable and effective across a significantly wider range, with the loss staying below 0.01 for η in 0.08 and 0.3.

Image regression. The problem setting follows that of Section 4. SGDL and MGDL are implemented using structures (28) and (32), respectively. The learning rate is selected from the interval $[0.001, 1]$, with training performed for 1×10^5 epochs.

Figure 15 illustrates the effect of learning rate on performance across four images: ‘Resolution Chart’, ‘Cameraman’, ‘Barbara’, and ‘Pirate’. In all cases, MGDL consistently achieves higher accuracy than SGDL. Notably, SGDL fails to train on the ‘Cameraman’ and ‘Pirate’ when the learning rate is near 1, while MGDL remains stable and continues to produce accurate results under these learning rates.

Numerical results on synthetic data regression and image regression demonstrate that MGDL is more robust to the choice of learning rate and performs well with larger learning rates compared to SGDL.

6 Eigenvalue Analysis for SGDL and MGDL

This section analyzes the GD method (2) applied to both SGDL and MGDL, as it is the most widely used approach for these optimization problems and serves as the foundation for many other methods.

GD can be viewed as a Picard iteration: $W^{k+1} = (\mathbf{I} - \eta \frac{\partial \mathcal{F}}{\partial W})(W^k)$, $k = 0, 1, \dots$, whose convergence is well-studied in fixed-point theory under nonexpansiveness assumptions [1]. However, when applied to deep learning, the resulting operator is typically expansive. To address this, we linearize $\frac{\partial \mathcal{F}}{\partial W}$ to facilitate the analysis of gradient descent behavior in deep networks.

Using the Taylor expansion at W^{k-1} , the gradient can be approximated as

$$\frac{\partial \mathcal{F}}{\partial W}(W^k) = \mathbf{H}_{\mathcal{F}}(W^{k-1})W^k + u^{k-1} + \frac{1}{2}(W^k - W^{k-1})^\top \mathbf{T}_{\mathcal{F}}(\bar{W})(W^k - W^{k-1}),$$

where $u^k := \frac{\partial \mathcal{F}}{\partial W}(W^k) - \mathbf{H}_{\mathcal{F}}(W^k)W^k$, $\mathbf{T}_{\mathcal{F}}(\bar{W})$ is the third derivative of \mathcal{F} at \bar{W} , and \bar{W} lies between W^k and W^{k-1} . Substituting into the GD update yields

$$W^{k+1} = \mathbf{A}^{k-1}W^k - \eta u^{k-1} + r^{k-1} \quad (6)$$

where $\mathbf{A}^{k-1} := \mathbf{I} - \eta \mathbf{H}_{\mathcal{F}}(W^{k-1})$ and $r^{k-1} := -\frac{\eta}{2}(W^k - W^{k-1})^\top \mathbf{T}_{\mathcal{F}}(\bar{W})(W^k - W^{k-1})$. Neglecting the remainder term r^{k-1} gives a linear approximation:

$$\tilde{W}^{k+1} = \mathbf{A}^{k-1}\tilde{W}^k - \eta u^{k-1}. \quad (7)$$

We next consider the convergence of the linearized GD (7), which depends on the spectral norm $\tau := \sup_{W \in \Omega} \|\mathbf{I} - \eta \mathbf{H}_{\mathcal{F}}(W)\|$ over a compact domain Ω . The proof is provided in Appendix B.

Theorem 4. *Suppose $\mathcal{F} : \mathbb{R}^M \rightarrow \mathbb{R}$ is a nonnegative, twice continuously differentiable and $\Omega \in \mathbb{R}^M$ is a convex, compact set. Let $\{\tilde{W}^k\}_{k=0}^\infty$ be generated by (7) and $\{W^k\}_{k=0}^\infty$ be generated by (6) and assume that $\{W^k\}_{k=0}^\infty \subset \Omega$. If $\tau < 1$, then the sequence $\{\tilde{W}^k\}_{k=0}^\infty$ converges.*

We establish the connection between the GD (6) and its linearization (7); see Appendix B for proof.

Theorem 5. *Suppose $\mathcal{F} : \mathbb{R}^M \rightarrow \mathbb{R}$ is a nonnegative, three times continuously differentiable function and $\Omega \in \mathbb{R}^M$ is a convex, compact set. Let the sequence $\{W^k\}_{k=0}^\infty$ be generated by (6), $\{\tilde{W}^k\}_{k=0}^\infty$ be generated by (7) with $\tilde{W}^0 = W^0$ and $\tilde{W}^1 = W^1$, and assume $\{W^k\}_{k=0}^\infty \subset \Omega$. If $\tau < 1$, then both $\{\tilde{W}^k\}_{k=0}^\infty$ and $\{W^k\}_{k=0}^\infty$ converge to the same point.*

Theorem 5 shows that the convergence of sequence $\{W^k\}_{k=1}^\infty$ is mainly governed by $\mathbf{I} - \eta \mathbf{H}_{\mathcal{F}}(W)$. A sufficient and practically verifiable condition for convergence is that all eigenvalues of this matrix lie within $(-1, 1)$. For numerical analysis, we provide the explicit Hessian of \mathcal{F} (with $\mathcal{F} := \mathcal{L}$ for SGDL and $\mathcal{F} := \mathcal{L}_l$ for MGDL) under ReLU activation in the Supplementary Material.

We next track the eigenvalues of $\mathbf{I} - \eta \mathbf{H}_{\mathcal{F}}(W^k)$ during training to study convergence. In deep networks like SGDL, these eigenvalues often fall outside $(-1, 1)$, leading to oscillatory loss. In contrast, MGDL’s shallow structure keeps them within $(-1, 1)$, yielding smooth loss decay.

Synthetic data regression. The problem settings—including target function, training/validation data, network structures, and activation function—are the same as in Section 5. We use gradient descent to optimize both models, selecting the learning rate η from the interval $[0.001, 0.5]$ based on the lowest validation loss. Numerical results are shown in Figure 2 (Setting 1) and Figure 16 (Setting 2).

We begin by analyzing SGDL under Setting 1. In Figure 2, the first subfigure shows the ten smallest (solid) and ten largest (dashed) eigenvalues of $\mathbf{I} - \eta \mathbf{H}_{\mathcal{L}}(W^k)$ over the training process (up to 10^6 epochs). The smallest eigenvalue (index 0) remains significantly below -1 , while eigenvalues with indices 1 through 5 stay below or near -1 . All ten largest eigenvalues remain slightly above 1, indicating limited influence on training dynamics. The third subfigure plots the loss function over training. While the loss decreases overall, it shows moderate oscillations in the first 10^5 epochs and stronger oscillations thereafter. These patterns align with the behavior of the smallest eigenvalues: moderate oscillations correspond to three eigenvalues below or near -1 , while stronger oscillations occur as more eigenvalues fall into this range. These results indicate that oscillations in the loss are closely linked to the number of eigenvalues of $\mathbf{I} - \eta \mathbf{H}_{\mathcal{L}}(W^k)$ that are less than or near -1 .

We next analyze MGDL for Setting 1. In Figure 2, the second subfigure shows the ten smallest (solid) and ten largest (dashed) eigenvalues of $\mathbf{I} - \eta \mathbf{H}_{\mathcal{L}}(W^k)$ during training. Nearly all of the smallest eigenvalues stay within $(-1, 1)$ across grades 1-4, while the largest eigenvalues remain slightly above 1. This behavior supports the stable loss reduction observed in the fourth subfigure.

Training behavior of both methods is influenced by the eigenvalues of $\mathbf{I} - \eta \mathbf{H}_{\mathcal{L}}(W^k)$. SGDL’s eigenvalue drops below or near -1 , causing loss oscillation, while MGDL’s eigenvalues remain within $(-1, 1)$, resulting in stable loss reduction. This shows that the MGDL improves training stability. As shown in the first two subfigures of Figure 17, both methods achieve similar accuracy.

We now turn to the numerical analysis of Setting 2, as shown in Figure 16. The target function in Setting 2 is similar to that in Setting 1, but it includes a higher-frequency component, making it more challenging to learn. For SGDL, the first subfigure shows eigenvalues of $\mathbf{I} - \eta \mathbf{H}_{\mathcal{L}}(W^k)$. At the initial 2×10^5 epochs, all eigenvalues fall in $(-1, 1)$. Therefore, the loss function decreases stably during this period, as shown in the third subfigure. After 2×10^5 epochs, the smallest eigenvalue (index 0), drops to -1 , and the second smallest eigenvalue approaches -1 . This causes the strong oscillations of the loss function during the period 2×10^5 to 10^6 . The oscillations become even stronger after 6×10^5 as the smallest eigenvalue drops -1 significantly and more eigenvalues approach or fall below -1 . For MGDL, the behavior of eigenvalues and the loss values, as shown in the second and fourth subfigures, are consistent with those in Setting 1. The third and fourth subfigures in Figure 17 illustrate MGDL achieves much better prediction accuracy than SGDL.

Both Settings 1 and 2 demonstrate that MGDL is more stable than SGDL. The instability of SGDL can be attributed to the eigenvalues of $\mathbf{I} - \eta \mathbf{H}_{\mathcal{L}}(W^k)$, where the eigenvalue drops below or approaches -1 during the training. For the same reason, the stability of MGDL is also explained by the eigenvalues of $\mathbf{I} - \eta \mathbf{H}_{\mathcal{L}}(W^k)$ where nearly all eigenvalues remain within the range $(-1, 1)$ throughout the training. Moreover, MGDL achieves significantly better accuracy in the more challenging Setting 2.

Across Settings 1 and 2 for both SGDL and MGDL, the smallest eigenvalue of $\mathbf{I} - \eta \mathbf{H}_{\mathcal{L}}(W^k)$ has a greater impact on the behavior of the loss function compared to the largest eigenvalue. This is because the largest eigenvalue is close to 1, contributing to the stability of the iteration. In contrast, when the smallest eigenvalue approaches or drops below -1 , the iteration tends to oscillate.

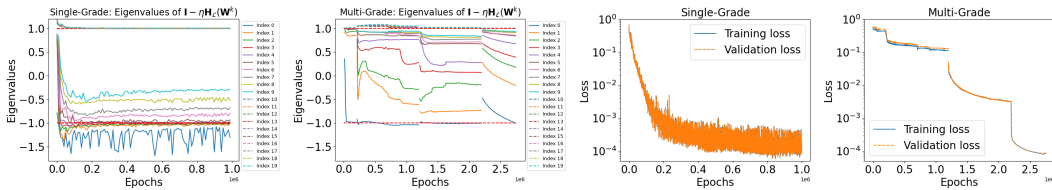


Figure 2: Training process of SGDL ($\eta = 0.08$) and MGDL ($\eta = 0.06$) for Setting 1.

Image regression. The problem setting follows Section 4. To facilitate Hessian computation for SGDL and MGDL, we adopt a shallow and narrow neural network. SGDL and MGDL follow the architectures in (27) and (31), respectively, and are optimized via gradient descent.

We conduct an eigenvalue analysis of SGDL and MGDL on the image regression task, using the images ‘Resolution chart’, ‘Cameraman’, ‘Barbara’, and ‘Butterfly’. Computing the Hessian matrix of the loss becomes computationally expensive when using all the pixels from images. To mitigate this, we train the models on a selected subset of pixels. Results are reported in Figures 3 and 18-20. The performance of SGDL and MGDL remains similar across the four images. For SGDL, when

only the smallest eigenvalue of $\mathbf{I} - \eta \mathbf{H}_{\mathcal{L}}(\mathbf{W}^k)$ is close to -1 , the loss exhibits slight oscillations, for example, during the initial 1.3×10^5 , 5×10^4 , 8×10^4 , and 2×10^5 epochs for the four images, respectively. When multiple eigenvalues approach -1 , the oscillations become more pronounced. For MGDL, all the eigenvalue of $\mathbf{I} - \eta \mathbf{H}_{\mathcal{L}}(\mathbf{W}^k)$ fall in $(-1, 1)$ across the four images, resulting in a stable decrease in loss across all images, as shown in Figures 3 and 18-20.

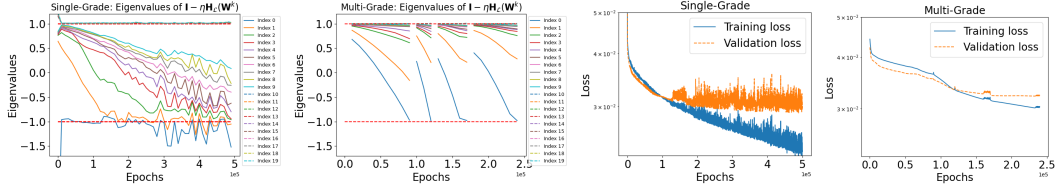


Figure 3: Training process of SGDL ($\eta = 0.02$) and MGDL ($\eta = 0.2$) for ‘Resolution chart’.

Image denoising. We consider the same problem setting in Section 4. SGDL and MGDL follow the architectures in (27) and (31), respectively, and are optimized via gradient descent.

The numerical results are reported in Figures 21-24. We observe that, for SGDL, the smallest eigenvalue approaches -1 , causing instability and oscillations in the loss function. In contrast, MGDL maintains all eigenvalues within $(-1, 1)$, ensuring a stable and steadily decreasing loss.

Numerical results, including synthetic data regression, image regression, and image denoising, consistently show that the eigenvalues of $\mathbf{I} - \eta \mathbf{H}_{\mathcal{L}}(\mathbf{W}^k)$ for SGDL tend to approach or fall below -1 , while those for MGDL are more likely to remain stable within the interval $(-1, 1)$. This behavior explains why MGDL exhibits greater stability compared to SGDL.

7 Comparison of MSDL and MGDL

This section compares multi-scale deep learning (MSDL) [21, 34] and MGDL on the synthetic data regression task, using the same problem setup described in Section 5. MGDL adopts the architecture defined in (30), while MSDL’s architecture—configured to match the total number of neurons—is provided in Appendix D. Both models employ ReLU activation functions and the shallow, narrow network are used to simplify the computation of Hessian eigenvalues. Training is performed using gradient descent, with the learning rate η selected from $[0.001, 0.5]$ to minimize validation loss.

Numerical comparisons between MSDL and MGDL are shown in Figures 25-26 for Settings 1 and 2. In both cases, MSDL exhibits more frequent occurrences of eigenvalues near or below -1 , causing oscillations in the training loss. MSDL’s predictions appear in Figure 27, and MGDL’s in Figure 17. Figure 28 highlights MSDL’s greater sensitivity to learning rate. Improved stability for MSDL may be possible with compactly supported activations and deeper, wider networks, as suggested in [21].

8 Conclusion

We conducted extensive numerical experiments on synthetic regression and image reconstruction tasks. The results consistently show that MGDL outperforms SGDL, with MGDL exhibiting stable training dynamics, while SGDL displays oscillatory behavior. To explain this, we analyzed the eigenvalues of the iteration matrices and established a convergence theorem for the GD method. The theorem confirms that the training dynamics are primarily governed by the eigenvalues of the iteration matrices. The numerical analysis reveals that SGDL’s eigenvalues frequently lie outside the interval $(-1, 1)$, leading to oscillatory training behavior, whereas MGDL’s remain within this range, contributing to its stable training dynamics. We also investigated the effect of learning rate and found that MGDL is more robust and performs well with a larger learning rate when compared with SGDL. These comparisons highlight the computational advantages and practical robustness of MGDL.

Limitation: We established convergence results for SGDL and MGDL within the gradient descent framework. However, widely used optimization algorithms such as SGD and Adam were not analyzed. While our numerical experiments demonstrate that MGDL achieves superior performance, improved training stability, and robustness to learning rate choices, the theoretical foundations of these advantages remain to be fully understood.

References

- [1] Heinz H Bauschke and Patrick L Combettes. *Convex Analysis and Monotone Operator Theory in Hilbert Spaces*. Springer, 2017.
- [2] Yoshua Bengio, Pascal Lamblin, Dan Popovici, and Hugo Larochelle. Greedy layer-wise training of deep networks. *Advances in neural information processing systems*, 19, 2006.
- [3] Tom Brown, Benjamin Mann, Nick Ryder, Melanie Subbiah, Jared D Kaplan, Prafulla Dhariwal, Arvind Neelakantan, Pranav Shyam, Girish Sastry, Amanda Askell, et al. Language models are few-shot learners. *Advances in neural information processing systems*, 33:1877–1901, 2020.
- [4] Hongming Chen, Ola Engkvist, Yinhai Wang, Marcus Olivecrona, and Thomas Blaschke. The rise of deep learning in drug discovery. *Drug discovery today*, 23(6):1241–1250, 2018.
- [5] Jeremy M Cohen, Simran Kaur, Yuanzhi Li, J Zico Kolter, and Ameet Talwalkar. Gradient descent on neural networks typically occurs at the edge of stability. *arXiv preprint arXiv:2103.00065*, 2021.
- [6] Tolga Ergen and Mert Pilanci. Convex geometry and duality of over-parameterized neural networks. *Journal of machine learning research*, 22(212):1–63, 2021.
- [7] Ronglong Fang and Yuesheng Xu. Addressing spectral bias of deep neural networks by multi-grade deep learning. In A. Globerson, L. Mackey, D. Belgrave, A. Fan, U. Paquet, J. Tomczak, and C. Zhang, editors, *Advances in Neural Information Processing Systems*, volume 37, pages 114122–114146. Curran Associates, Inc., 2024. URL https://proceedings.neurips.cc/paper_files/paper/2024/file/cf1129594f603fde9e1913d10b7dbf77-Paper-Conference.pdf.
- [8] Ronglong Fang, Yuesheng Xu, and Mingsong Yan. Inexact fixed-point proximity algorithm for the ℓ_0 sparse regularization problem. *Journal of Scientific Computing*, 100(2):58, 2024.
- [9] Xavier Glorot and Yoshua Bengio. Understanding the difficulty of training deep feedforward neural networks. In *Proceedings of the thirteenth international conference on artificial intelligence and statistics*, pages 249–256. JMLR Workshop and Conference Proceedings, 2010.
- [10] Ian Goodfellow, Yoshua Bengio, Aaron Courville, and Yoshua Bengio. *Deep learning*, volume 1. MIT press Cambridge, 2016.
- [11] Jianfeng Guo, C Ross Schmidlein, Andrzej Krol, Si Li, Yizun Lin, Sangtae Ahn, Charles Stearns, and Yuesheng Xu. A fast convergent ordered-subsets algorithm with subiteration-dependent preconditioners for pet image reconstruction. *IEEE transactions on medical imaging*, 41(11):3289–3300, 2022.
- [12] Kaiming He, Xiangyu Zhang, Shaoqing Ren, and Jian Sun. Deep residual learning for image recognition. In *Proceedings of the IEEE conference on computer vision and pattern recognition*, pages 770–778, 2016.
- [13] Sepp Hochreiter and Jürgen Schmidhuber. Long short-term memory. *Neural computation*, 9(8):1735–1780, 1997.
- [14] Jie Jiang and Yuesheng Xu. Deep neural network solutions for oscillatory fredholm integral equations. *Journal of Integral Equations and Applications*, 36(1):23–55, 2024.
- [15] John Jumper, Richard Evans, Alexander Pritzel, Tim Green, Michael Figurnov, Olaf Ronneberger, Kathryn Tunyasuvunakool, Russ Bates, Augustin Žídek, Anna Potapenko, et al. Highly accurate protein structure prediction with alphafold. *nature*, 596(7873):583–589, 2021.
- [16] Jack Kiefer and Jacob Wolfowitz. Stochastic estimation of the maximum of a regression function. *The Annals of Mathematical Statistics*, pages 462–466, 1952.
- [17] D.P. Kingma and J. Ba. Adam: A method for stochastic optimization. In *Proceedings of the 3rd International Conference on Learning Representations (ICLR)*, 2015. URL <https://arxiv.org/abs/1412.6980>.

- [18] Alex Krizhevsky, Ilya Sutskever, and Geoffrey E Hinton. Imagenet classification with deep convolutional neural networks. *Advances in neural information processing systems*, 25, 2012.
- [19] Yann LeCun, Léon Bottou, Yoshua Bengio, and Patrick Haffner. Gradient-based learning applied to document recognition. *Proceedings of the IEEE*, 86(11):2278–2324, 1998.
- [20] Qia Li, Lixin Shen, Yuesheng Xu, and Na Zhang. Multi-step fixed-point proximity algorithms for solving a class of optimization problems arising from image processing. *Advances in Computational Mathematics*, 41(2):387–422, 2015.
- [21] Ziqi Liu, Wei Cai, and Zhi-Qin John Xu. Multi-scale deep neural network (mscalednn) for solving poisson-boltzmann equation in complex domains. *Communications in Computational Physics*, 28:1970–2001, 2020.
- [22] Charles A Micchelli, Lixin Shen, and Yuesheng Xu. Proximity algorithms for image models: denoising. *Inverse Problems*, 27(4):045009, 2011.
- [23] Charles A Micchelli, Lixin Shen, Yuesheng Xu, and Xueying Zeng. Proximity algorithms for the 11/tv image denoising model. *Advances in Computational Mathematics*, 38:401–426, 2013.
- [24] Razvan Pascanu, Tomas Mikolov, and Yoshua Bengio. On the difficulty of training recurrent neural networks. In *International conference on machine learning*, pages 1310–1318. Pmlr, 2013.
- [25] Mert Pilanci and Tolga Ergen. Neural networks are convex regularizers: Exact polynomial-time convex optimization formulations for two-layer networks. In *International Conference on Machine Learning*, pages 7695–7705. PMLR, 2020.
- [26] Nasim Rahaman, Aristide Baratin, Devansh Arpit, Felix Draxler, Min Lin, Fred Hamprecht, Yoshua Bengio, and Aaron Courville. On the spectral bias of neural networks. In *International conference on machine learning*, pages 5301–5310. PMLR, 2019.
- [27] Maziar Raissi, Paris Perdikaris, and George E Karniadakis. Physics-informed neural networks: A deep learning framework for solving forward and inverse problems involving nonlinear partial differential equations. *Journal of Computational physics*, 378:686–707, 2019.
- [28] Herbert Robbins and Sutton Monro. A stochastic approximation method. *The annals of mathematical statistics*, pages 400–407, 1951.
- [29] Leonid I Rudin, Stanley Osher, and Emad Fatemi. Nonlinear total variation based noise removal algorithms. *Physica D: nonlinear phenomena*, 60(1-4):259–268, 1992.
- [30] Lixin Shen, Yuesheng Xu, and Xueying Zeng. Wavelet inpainting with the ℓ_0 sparse regularization. *Applied and Computational Harmonic Analysis*, 41(1):26–53, 2016.
- [31] Alex Sherstinsky. Fundamentals of recurrent neural network (rnn) and long short-term memory (lstm) network. *Physica D: Nonlinear Phenomena*, 404:132306, 2020.
- [32] Karen Simonyan and Andrew Zisserman. Very deep convolutional networks for large-scale image recognition. In *3rd International Conference on Learning Representations (ICLR 2015)*, pages 1–14, 2015.
- [33] Ashish Vaswani, Noam Shazeer, Niki Parmar, Jakob Uszkoreit, Llion Jones, Aidan N Gomez, Łukasz Kaiser, and Illia Polosukhin. Attention is all you need. *Advances in neural information processing systems*, 30, 2017.
- [34] Bo Wang, Wenzhong Zhang, and Wei Cai. Multi-scale deep neural network (mscalednn) methods for oscillatory stokes flows in complex domains. *Communications in Computational Physics*, 28:2139–2157, 2020.
- [35] Tingting Wu and Yuesheng Xu. Inverting incomplete fourier transforms by a sparse regularization model and applications in seismic wavefield modeling. *Journal of Scientific Computing*, 92(2):48, 2022.

- [36] Yuesheng Xu. Successive affine learning for deep neural networks. *Analysis and Applications, to appear. arXiv preprint arXiv:2305.07996*, 2023.
- [37] Yuesheng Xu. Multi-grade deep learning. *Communications on Applied Mathematics and Computation*, pages 1–52, 2025.
- [38] Yuesheng Xu and Taishan Zeng. Multi-grade deep learning for partial differential equations with applications to the burgers equation. *arXiv preprint arXiv:2309.07401*, 2023.
- [39] Zhi-Qin John Xu, Yaoyu Zhang, and Yanyang Xiao. Training behavior of deep neural network in frequency domain. In *Neural Information Processing: 26th International Conference, ICONIP 2019, Sydney, NSW, Australia, December 12–15, 2019, Proceedings, Part I 26*, pages 264–274. Springer, 2019.

A Convex Program Formulation for MGDL

We briefly formulate the convex program for MGDL, where each grade is a two-layer ReLU network. For detailed discussions, see [25].

A two-layer ReLU network function at grade l , $\mathcal{N}_{2l} : \mathbb{R}^{d_l} \rightarrow \mathbb{R}$, with m_l neurons, is defined as

$$\mathcal{N}_{2l}(\mathbf{x}_l) = \sum_{j=1}^{m_l} \alpha_{lj} (\mathbf{w}_{lj}^\top \mathbf{x}_l)_+,$$

where \mathbf{x}_l is the input feature for grade l , \mathbf{w}_{lj} and α_{lj} are parameters at the first and second layers. Let data matrix be $\mathbf{X}_l := [\mathbf{x}_{l1}, \mathbf{x}_{l2}, \dots, \mathbf{x}_{lN}]^\top \in \mathbb{R}^{N \times d_l}$, the residual vector be $\mathbf{e}_l := [\mathbf{e}_{l1}, \mathbf{e}_{l2}, \dots, \mathbf{e}_{lN}]^\top \in \mathbb{R}^N$, and let $\beta_l > 0$ be a regularization parameter. Consider minimizing the squared loss objective and squared ℓ_2 -norm of all parameters

$$\min_{\{\mathbf{w}_{lj}, \alpha_{lj}\}_{j=1}^{m_l}} \frac{1}{2} \left\| \sum_{j=1}^{m_l} \alpha_{lj} (\mathbf{X}_l \mathbf{w}_{lj})_+ - \mathbf{e}_l \right\|^2 + \frac{\beta_l}{2} \sum_{j=1}^{m_l} \left(\|\mathbf{w}_{lj}\|^2 + \alpha_{lj}^2 \right). \quad (8)$$

We next state the corresponding convex program. Consider diagonal matrices $\text{Diag}(1[\mathbf{X}_l \mathbf{w}_l \geq 0])$ where $\mathbf{w}_l \in \mathbb{R}^{d_l}$ is arbitrary and $1[\mathbf{X}_l \mathbf{w}_l \geq 0] \in \{0, 1\}^N$ is an indicator vector with Boolean elements $[1[\mathbf{x}_{l1}^\top \mathbf{w}_l \geq 0], \dots, 1[\mathbf{x}_{lN}^\top \mathbf{w}_l \geq 0]]$. Let us enumerate all such distinct diagonal matrices that can be obtained for all possible $\mathbf{w}_l \in \mathbb{R}^{d_l}$, and denote them as $\mathbf{D}_{l1}, \dots, \mathbf{D}_{lP_l}$. P_l is the number of regions in a partition of \mathbb{R}^{d_l} by hyperplanes passing through the origin, and are perpendicular to the rows of \mathbf{X}_l . The convex program is

$$\min_{\{\mathbf{u}_{li}, \mathbf{v}_{li}\}_{i=1}^{P_l}} \frac{1}{2} \left\| \sum_{i=1}^{P_l} \mathbf{D}_{li} \mathbf{X}_l (\mathbf{u}_{li} - \mathbf{v}_{li}) - \mathbf{e}_l \right\|^2 + \beta_l \sum_{i=1}^{P_l} (\|\mathbf{u}_{li}\| + \|\mathbf{v}_{li}\|) \quad (9)$$

$$\text{s.t. } (2\mathbf{D}_{li} - \mathbf{I}_N) \mathbf{X}_l \mathbf{u}_{li} \geq 0, (2\mathbf{D}_{li} - \mathbf{I}_N) \mathbf{X}_l \mathbf{v}_{li} \geq 0, i \in \mathbb{N}_{P_l}.$$

B Convergence Proof

Proofs of Theorem 1 and Theorem 2

We begin by establishing the convergence of the general gradient descent iteration 2, which serves as the foundation for the proofs of Theorems 1 and 2. For a compact convex set $\Omega \in \mathbb{R}^M$, we let

$$\alpha := \sup_{W \in \Omega} \|\mathbf{H}_{\mathcal{F}}(W)\| \quad (10)$$

where $\|\cdot\|$ is the spectral norm of a matrix.

Theorem 6. *Suppose $\mathcal{F} : \mathbb{R}^M \rightarrow \mathbb{R}$ is a nonnegative, twice continuously differentiable function and $\Omega \in \mathbb{R}^M$ is a convex, compact set. Let $\{W^k\}_{k=1}^\infty$ be a sequence generate from (2) for a given initial guess W^0 and assume that $\{W^k\}_{k=1}^\infty \subset \Omega$. If the learning rate $\eta \in (0, 2/\alpha)$, then the following statements hold:*

- (i) $\lim_{k \rightarrow \infty} \mathcal{F}(W^k) = F^*$ for some $F^* \geq 0$;
- (ii) $\lim_{k \rightarrow \infty} \frac{\partial \mathcal{F}}{\partial \bar{W}}(W^k) = 0$ and $\lim_{k \rightarrow \infty} \|W^{k+1} - W^k\| = 0$;
- (iii) Every cluster point \hat{W} of $\{W^k\}_{k=0}^\infty$ satisfies $\frac{\partial \mathcal{F}}{\partial \bar{W}}(\hat{W}) = 0$.

Proof. Since \mathcal{F} is twice continuously differentiable, we can expand $\mathcal{F}(W^{k+1})$ at W^k yields

$$\mathcal{F}(W^{k+1}) = \mathcal{F}(W^k) + \left(\frac{\partial \mathcal{F}}{\partial \bar{W}} \right)^\top (W^k) \Delta W^k + r_k$$

with an error term

$$r_k = \frac{1}{2} (\Delta W^k)^\top \mathbf{H}_{\mathcal{F}}(\bar{W}) \Delta W^k$$

where $\Delta W^k = W^{k+1} - W^k$ and \bar{W} is a point between W^k and W^{k+1} . By using equation (2), we have that

$$\frac{\partial \mathcal{F}}{\partial \bar{W}}(W^k) = -\frac{1}{\eta} \Delta W^k. \quad (11)$$

Therefore,

$$\mathcal{F}(W^{k+1}) = \mathcal{F}(W^k) - \frac{1}{\eta} \|\Delta W^k\|^2 + r_k \quad (12)$$

We next estimate r_k . Since \mathcal{F} is twice continuously differentiable, $\mathbf{H}_{\mathcal{F}}$ is continuous. As Ω is compact, $\mathbf{H}_{\mathcal{F}}$ is also bounded on Ω . Moreover, since both W^{k+1} and W^k are in the convex set Ω , we have that $\bar{W} \in \Omega$. It follows from (10) and compactness of Ω that

$$r_k \leq \frac{\alpha}{2} \|\Delta W^k\|^2.$$

Substituting the above inequality into the right-hand side of equation (12), we have that

$$\mathcal{F}(W^{k+1}) \leq \mathcal{F}(W^k) - \left(\frac{1}{\eta} - \frac{\alpha}{2} \right) \|\Delta W^k\|^2. \quad (13)$$

Since $\eta \in (0, \frac{2}{\alpha})$, we have that $\frac{1}{\eta} - \frac{\alpha}{2} > 0$. The nonnegativity of $\frac{1}{\eta} - \frac{\alpha}{2}$ yields

$$0 \leq \mathcal{F}(W^{k+1}) \leq \mathcal{F}(W^k), \text{ for } k = 0, 2, \dots$$

This guarantees that $\{\mathcal{F}(W^k)\}_{k=0}^\infty$ is a convergent sequence, thereby establishing Item (i).

We next prove Item (ii). For any positive integer K , summing inequality (13) over $k = 0, 1, \dots, K$ and then we get

$$\sum_{k=0}^K \left(\frac{1}{\eta} - \frac{\alpha}{2} \right) \|\Delta W^k\|^2 \leq \mathcal{F}(W^0) - \mathcal{F}(W^{K+1}) \leq \mathcal{F}(W^0).$$

Since $\frac{1}{\eta} - \frac{\alpha}{2}$ is positive, the above inequality implies that

$$\sum_{k=0}^{\infty} \|\Delta W^k\|^2 < \infty.$$

Therefore,

$$\lim_{k \rightarrow \infty} \|\Delta W^k\| = 0. \quad (14)$$

Equation (11) yields that

$$\lim_{k \rightarrow \infty} \left\| \frac{\partial \mathcal{F}}{\partial \bar{W}}(W^k) \right\| = 0 \quad (15)$$

and

$$\lim_{k \rightarrow \infty} \|W^{k+1} - W^k\| = 0$$

which estimates Item (ii).

We next show Item (iii). Let \hat{W} be a cluster point of $\{W^k\}_{k=0}^\infty$. Then there exists a subsequence $\{W^{k_i}\}_{i=0}^\infty$ of $\{W^k\}_{k=0}^\infty$ such that $\lim_{i \rightarrow \infty} W^{k_i} = \hat{W}$. The continuous of the gradient with Item (ii) implies that

$$\frac{\partial \mathcal{F}}{\partial \bar{W}}(\hat{W}) = \lim_{i \rightarrow \infty} \frac{\partial \mathcal{F}}{\partial \bar{W}}(W^{k_i}) = 0,$$

which proves Item (iii). \square

Lemma 7. *Suppose that the activation function σ is twice continuously differentiable and the loss function \mathcal{L} is defined by (1), then the gradient $\frac{\partial \mathcal{L}}{\partial \mathbf{W}}$ and hessian $\mathbf{H}_{\mathcal{L}}$ are continuous.*

Proof. The key point of the proof is that a polynomial of a continuous function is continuous and so is a composition of continuous function.

It follows from Lemma 3 of [37] that the componetwise of $\frac{\partial \mathcal{L}}{\partial \mathbf{W}}$ and $\mathbf{H}_{\mathcal{L}}$ are polynomials of $\sigma, \sigma', \{\mathbf{x}_\ell, \mathbf{y}_\ell\}_{\ell=1}^N$ and the composition of $\sigma, \sigma', \sigma''$. These ensure that $\frac{\partial \mathcal{L}}{\partial \mathbf{W}}$ and $\mathbf{H}_{\mathcal{L}}$ are continuous. \square

proof of Theorem 1. We apply Theorem 6 with $\mathcal{F} := \mathcal{L}$. Under the hypothesis that σ is twice continuously differentiable, we have shown in Lemma 7 that the gradient $\frac{\partial \mathcal{L}}{\partial \mathbf{W}}$ and $\mathbf{H}_{\mathcal{L}}$ are continuous. Therefore, \mathcal{L} is twice continuously differentiable. It follows from the continuity of $\mathbf{H}_{\mathcal{L}}$ and the compactness of the domain \mathcal{W} that α is finite. Thus, the hypothesis of Theorem 6 is satisfied with $\mathcal{F} := \mathcal{L}$. Theorem 1 is a direct consequence of Theorem 6. \square

Lemma 8. *Suppose that the activation function σ is twice continuously differentiable and the loss function \mathcal{L}_l is defined by (3) with $\{\mathbf{x}_{l\ell}, \mathbf{e}_{l\ell}\}_{\ell=1}^N$ being bounded, then the gradient $\frac{\partial \mathcal{L}_l}{\partial \mathbf{W}_l}$ and hessian $\mathbf{H}_{\mathcal{L}_l}$ are continuous.*

Proof. Since grade l in MGD is essentially a traditional shallow neural network with the only change being the training data, which is replaced by $\{\mathbf{x}_{l\ell}, \mathbf{e}_{l\ell}\}_{\ell=1}^N$. We further assume that $\{\mathbf{x}_{l\ell}, \mathbf{e}_{l\ell}\}_{\ell=1}^N$ is bounded. This change does not affect the continuity of the gradient and Hessian. Consequently, this lemma follows directly from Lemma 7. \square

Proof of Theorem 2. We apply Theorem 6 with $\mathcal{F} := \mathcal{L}_l$. Under the hypothesis that σ is twice continuously differentiable, we have shown in Lemma 8 that the gradient $\frac{\partial \mathcal{L}_l}{\partial \mathbf{W}_l}$ and $\mathbf{H}_{\mathcal{L}_l}$ are continuous. Therefore, \mathcal{L}_l is twice continuously differentiable. It follows from the continuity of $\mathbf{H}_{\mathcal{L}_l}$ and the compactness of the domain \mathcal{W}_l that α is finite. Thus, the hypothesis of Theorem 6 is satisfied with $\mathcal{F} := \mathcal{L}_l$. Theorem 2 is a direct consequence of Theorem 6. \square

Proofs of Theorem 4 and Theorem 5

Proof of Theorem 4. The linear approximation of the gradient descent method (7) can be expressed as

$$\tilde{W}^{k+1} = \left(\prod_{j=0}^{k-1} \mathbf{A}^j \right) \tilde{W}^1 - \eta \sum_{m=0}^{k-1} \left(\prod_{j=m+1}^{k-1} \mathbf{A}^j \right) u^m. \quad (16)$$

To establish the convergence of \tilde{W}^{k+1} , it suffices to demonstrate that the two terms on the right-hand side of (16) converge separately.

We first show the first term. By the definition of τ , we have that $\|\mathbf{A}^k\| \leq \tau$ for each k . By using the property of norm, we have that

$$\left\| \left(\prod_{j=0}^{k-1} \mathbf{A}^j \right) \tilde{W}^1 \right\| \leq \left(\prod_{j=0}^{k-1} \|\mathbf{A}^j\| \right) \|\tilde{W}^1\| \leq \tau^{k-1} \|\tilde{W}^1\|.$$

The first term of the right-hand side of (16) converges to zero as $k \rightarrow \infty$.

We next show the convergence of the second term of the right-hand side of (16). We first show that u^k is bound for each k . Since \mathcal{F} is twice continuously differentiable, we have that $\frac{\partial \mathcal{F}}{\partial \mathbf{W}}(W)$ and $\mathbf{H}_{\mathcal{F}}(W)$ are continuous. By using the condition $\{W^k\} \subset \Omega$ and Ω is compact, we obtain that $u^k := \frac{\partial \mathcal{F}}{\partial \mathbf{W}}(W^k) - \mathbf{H}_{\mathcal{F}}(W^k)W^k$ is also bounded for each k . Suppose u^k is bounded by C for all k . Then we have that

$$\left\| \left(\prod_{j=m+1}^{k-1} \mathbf{A}^j \right) u^m \right\| \leq \tau^{k-1-m} C.$$

Hence,

$$\sum_{m=0}^{k-1} \left\| \left(\prod_{j=m+1}^{k-1} \mathbf{A}^j \right) u^m \right\| \leq C \sum_{m=0}^{k-1} \tau^{k-1-m} = C \frac{1 - \tau^k}{1 - \tau}.$$

As $k \rightarrow \infty$, we have that

$$\left\| \sum_{m=0}^{\infty} \left(\prod_{j=m+1}^{\infty} \mathbf{A}^j \right) u^m \right\| \leq \sum_{m=0}^{\infty} \left\| \left(\prod_{j=m+1}^{\infty} \mathbf{A}^j \right) u^m \right\| \leq \frac{C}{1 - \tau},$$

which proves the second term of the right-hand side of (16) converges. \square

Lemma 9. *Suppose $\mathcal{F} : \mathbb{R}^M \rightarrow \mathbb{R}$ is a nonnegative, twice continuously differentiable function and $\Omega \in \mathbb{R}^M$ is a convex, compact set. If $\tau < 1$ for all $W \in \Omega$, then $\eta \in (0, 2/\alpha)$ with α defined in (10).*

Proof. Let $W \in \Omega$, and let $\lambda_1(W), \dots, \lambda_M(W)$ denote the eigenvalue of $\mathbf{H}_{\mathcal{F}}(W)$. By the definition of τ , we have

$$|1 - \eta \lambda_j(W)| \leq \tau, \text{ for all } W \in \Omega, \text{ and } j \in \mathbb{N}_M.$$

Since $\tau < 1$, it follows that $\lambda_j(W) > 0$ and

$$\eta \lambda_j(W) \leq 1 + \tau, \text{ for all } W \in \Omega, \text{ and } j \in \mathbb{N}_M.$$

Recalling the definition of α , we obtain

$$\eta \alpha \leq 1 + \tau.$$

Since $\tau < 1$, we have that $\eta \in (0, 2/\alpha)$, which completes the proof. \square

Proof of Theorem 5. The gradient descent iteration (6) can be expressed as

$$W^{k+1} = \left(\prod_{j=0}^{k-1} \mathbf{A}^j \right) W^1 - \eta \sum_{m=0}^{k-1} \left(\prod_{j=m+1}^{k-1} \mathbf{A}^j \right) u^m + \sum_{m=0}^{k-1} \left(\prod_{j=m+1}^{k-1} \mathbf{A}^j \right) r^m. \quad (17)$$

To establish the theorem, it suffices to demonstrate that the last term on the right-hand side of (17) converges to zero.

We first show that $\|r^k\|$ converges to zero. From Lemma 9, $\tau < 1$ includes $\eta \in (0, 2/\alpha)$. Thus, the hypothesis of Theorem 6 is satisfied. From the Item (ii) of Theorem 6, we have that $\lim_{k \rightarrow \infty} \|W^{k+1} - W^k\| = 0$. Since \mathcal{F} is three times continuously differentiable, $\mathbf{T}_{\mathcal{F}}$ is continuous. As Ω is compact, $\mathbf{T}_{\mathcal{F}}$ is also bounded on Ω ; let its spectral norm be bounded by C . Moreover, since both W^{k+1} and W^k are in the convex set Ω , we have that $\bar{W} \in \Omega$. Therefore

$$\|r^k\| \leq \frac{\eta C}{2} \|W^{k+1} - W^k\|^2.$$

By using $\lim_{k \rightarrow \infty} \|W^{k+1} - W^k\| = 0$, we have $\lim_{k \rightarrow \infty} \|r^k\| = 0$.

Since $\|r^k\|$ converges to zero, for any $\epsilon > 0$, there exists an N such that for all $k > N$, $\|r^k\| < \epsilon$. We split the last term on the right-hand side of (17) into two parts: from $m = 0$ to $N - 1$ and from N to $k - 1$.

For the first part ($m < N$), we have that

$$\left\| \sum_{m=0}^{N-1} \left(\prod_{j=m+1}^{k-1} \mathbf{A}^j \right) r^m \right\| \leq \sum_{m=0}^{N-1} \tau^{k-1-m} \|r^m\|.$$

As $k \rightarrow \infty$, τ^{k-1-m} converges to zero for each m , so the entire sum converges to zero. Therefore, we can find a integer K such that for all $k \geq K$

$$\left\| \sum_{m=0}^{N-1} \left(\prod_{j=m+1}^{k-1} \mathbf{A}^j \right) r^m \right\| < \epsilon.$$

For the second part ($m \geq N$):

$$\left\| \sum_{m=N}^{k-1} \left(\prod_{j=m+1}^{k-1} \mathbf{A}^j \right) r^m \right\| \leq \sum_{m=N}^{k-1} \tau^{k-1-m} \|r^k\| \leq \epsilon \sum_{m=N}^{k-1} \tau^{k-1-m} \leq \frac{\epsilon}{1-\tau}.$$

Therefore, for all $k > K$, we have that

$$\left\| \sum_{m=0}^{k-1} \left(\prod_{j=m+1}^{k-1} \mathbf{A}^j \right) r^m \right\| \leq \epsilon + \frac{\epsilon}{1-\tau}.$$

As ϵ is any positive number, the last term on the right-hand side of (17) converges to zero, which completes the proof of the theorem. \square

C Optimization Problem for Image Reconstruction

This appendix provides the optimization problems for solving image reconstruction tasks, including image denoising and deblurring.

Image denoising and deblurring are fundamental problems in image processing and have been extensively studied in the literature, as demonstrated in works such as [20, 22, 23]. These problems can be modeled as

$$\hat{\mathbf{f}} := \mathbf{A}\mathbf{f} + \epsilon$$

where $\hat{\mathbf{f}} \in \mathbb{R}^{n \times n}$ denotes the observed corrupted image, \mathbf{A} is a transform operator, $\mathbf{f} \in \mathbb{R}^{n \times n}$ is the ground truth image, and ϵ is the noise involved in the observed image. When \mathbf{A} is the identity transform, the model reduces to an image denoising problem [22, 23]; when \mathbf{A} represents a blurring operator, it corresponds to an image deblurring problem [8]. The statistical nature of the noise ϵ depends on the specific application: for instance, Gaussian noise is commonly used for natural images [22, 23], while Poisson noise is typical in medical imaging [11]. In this paper, we focus on the case where \mathbf{A} is a Gaussian blurring operator and ϵ is additive Gaussian noise.

We adopt the Rudin–Osher–Fatemi (ROF) total variation model [29], one of the most widely used models in image processing, to formalize the optimization problem. We view the gray scale image as a two-dimensional function $f : \mathbb{R}^2 \rightarrow \mathbb{R}$ from pixel coordinates to intensity values. The goal is to recover the underlying function f from the observed corrupted image $\hat{\mathbf{f}}$ using neural network-based function approximators. We begin by employing the SGDL framework to reconstruct the function f .

C.1 Problem Formalization for SGDL

Let $\mathcal{N}_D(\Theta; \mathbf{x})$ denote the SGDL function, we define the corresponding image matrix $\mathbf{N}_\Theta \in \mathbb{R}^{n \times n}$ be given by $[\mathbf{N}_\Theta]_{i,j} := \mathcal{N}_D(\Theta; \mathbf{x}_{i,j})$. The objective function is

$$\mathcal{G}(\Theta) := \frac{1}{2} \|\hat{\mathbf{f}} - \mathbf{A}\mathbf{N}_\Theta\|_{\text{F}}^2 + \lambda \|\mathbf{B}\mathbf{N}_\Theta\|_{1,1} \quad (18)$$

where \mathbf{B} denotes the first-order difference operator used to produce total-variation, as described in [22]. The norm $\|\cdot\|_{\text{F}}$ denotes the Frobenius norm of a matrix, which is the ℓ_2 norm of the vectorized form. The norm $\|\cdot\|_{1,1}$ denotes the entrywise ℓ_1 norm of a matrix, defined as the ℓ_1 norm of its vectorized form. The regularization parameter $\lambda > 0$ balances the trade-off between data fidelity and regularization. Since the objective function (18) involves a non-differentiable term $\|\cdot\|_{1,1}$ composed with the operator \mathbf{B} , minimizing (18) is challenging, as discussed in [8]. To address this issue, following the approach in [8, 30, 35], we introduce an auxiliary variable \mathbf{u} to free $\mathbf{B}\mathbf{N}_\Theta$ for the non-differentiable norm $\|\cdot\|_{1,1}$ and add the difference between \mathbf{u} and $\mathbf{B}\mathbf{N}_\Theta$ as a penalized term, resulting the following objective function:

$$\mathcal{L}(\Theta, \mathbf{u}) := \frac{1}{2} \|\hat{\mathbf{f}} - \mathbf{A}\mathbf{N}_\Theta\|_{\text{F}}^2 + \frac{\beta}{2} \|\mathbf{u} - \mathbf{B}\mathbf{N}_\Theta\|_{\text{F}}^2 + \lambda \|\mathbf{u}\|_{1,1}.$$

The optimization problem to reconstruct the underlying function can be formulated as

$$\operatorname{argmin} \{ \mathcal{L}(\Theta, \mathbf{u}) : \Theta \in \mathbb{R}^{M_D}, \mathbf{u} \in \mathbb{R}^{2n \times n} \}. \quad (19)$$

Since \mathcal{L} is non-differentiable with respect to \mathbf{u} and differentiable with respect to Θ , we use the proximity operator to update \mathbf{u} and use gradient-based method to update Θ . The resulting proximity-gradient algorithm is

$$\mathbf{u}^{k+1} = \text{prox}_{\alpha\lambda/\beta\|\cdot\|_{1,1}} \left(\alpha \mathbf{B} \mathbf{N}_{\Theta^k} + (1 - \alpha) \mathbf{u}^k \right), \quad (20)$$

$$\text{Using Adam optimizer to minimize } \mathcal{L}(\Theta, \mathbf{u}^{k+1}) \text{ and obtain } \Theta^{k+1}. \quad (21)$$

C.2 Problem Formalization for MGDL

We now employ the MGDL framework to reconstruct the function f . Grade 1 for MGDL is the same as for SGDL; the only difference is that the hidden layer is relatively smaller. We let

$$\mathcal{L}_1(\Theta_1, \mathbf{u}) := \frac{1}{2} \|\hat{\mathbf{f}} - \mathbf{A} \mathbf{N}_{\Theta_1}\|_{\text{F}}^2 + \frac{\beta}{2} \|\mathbf{u} - \mathbf{B} \mathbf{N}_{\Theta_1}\|_{\text{F}}^2 + \lambda \|\mathbf{u}\|_{1,1}. \quad (22)$$

The optimization problem can be formulated as

$$\text{argmin} \{ \mathcal{L}_1(\Theta_1, \mathbf{u}) : \Theta_1 \in \mathbb{R}^{M_{D_1}}, \mathbf{u} \in \mathbb{R}^{2n \times n} \}. \quad (23)$$

For grade l with $l \geq 2$, we will learn a new function \mathcal{N}_{D_l} which composite with $\mathcal{H}_{D_{l-1}-1}(\Theta_{l-1}^*; \cdot) \circ \dots \circ \mathcal{H}_{D_1-1}(\Theta_1^*; \cdot)$. Let $[\mathbf{g}_{\Theta_1^*}]_{i,j} := \mathcal{N}_{D_1}(\Theta_1^*; \mathbf{x}_{i,j})$ and

$$[\mathbf{g}_{\Theta_l}]_{i,j} := \epsilon_l \mathcal{N}_{D_l}(\Theta_l; \cdot) \circ \mathcal{H}_{D_{l-1}-1}(\Theta_{l-1}^*; \cdot) \circ \dots \circ \mathcal{H}_{D_1-1}(\Theta_1^*; \mathbf{x}_{i,j}) + [\mathbf{g}_{\Theta_{l-1}^*}]_{i,j}$$

where ϵ_l is a given normalization parameter, then the loss for grade l is

$$\mathcal{L}_l(\Theta_l, \mathbf{u}) := \frac{1}{2} \|\hat{\mathbf{f}} - \mathbf{A} \mathbf{g}_{\Theta_l}\|_{\text{F}}^2 + \frac{\beta}{2} \|\mathbf{u} - \mathbf{B} \mathbf{g}_{\Theta_l}\|_{\text{F}}^2 + \lambda \|\mathbf{u}\|_{1,1}. \quad (24)$$

The minimization problem for grade l can be formulated as

$$\text{argmin} \{ \mathcal{L}_l(\Theta_l, \mathbf{u}) : \Theta_l \in \mathbb{R}^{M_{D_l}}, \mathbf{u} \in \mathbb{R}^{2n \times n} \}. \quad (25)$$

Both optimization problems (23) and (25) are solved using the proximity-gradient algorithm (20)–(21), with the objective function replaced accordingly.

D Network Structures

This Appendix provides the network structures used in the paper.

For SGDL, we use the following network structures:

$$[1] \rightarrow [32] \times 4 \rightarrow [1], \quad (26)$$

$$[2] \rightarrow [48] \times 4 \rightarrow [1], \quad (27)$$

$$[2] \rightarrow [128] \times 8 \rightarrow [1], \quad (28)$$

$$[2] \rightarrow [128] \times 12 \rightarrow [1], \quad (29)$$

where $[n] \times N$ indicates N hidden layers, each with n neurons. The corresponding network structures for MGDL are:

$$\begin{aligned} \text{Grade 1 : } & [1] \rightarrow [32] \rightarrow [1] \\ \text{Grade 2 : } & [1] \rightarrow [32]_{\text{F}} \rightarrow [32] \rightarrow [1] \\ \text{Grade 3 : } & [1] \rightarrow [32]_{\text{F}} \times 2 \rightarrow [32] \rightarrow [1] \\ \text{Grade 4 : } & [1] \rightarrow [32]_{\text{F}} \times 3 \rightarrow [32] \rightarrow [1]. \end{aligned} \quad (30)$$

$$\begin{aligned} \text{Grade 1 : } & [2] \rightarrow [48] \rightarrow [1] \\ \text{Grade 2 : } & [2] \rightarrow [48]_{\text{F}} \rightarrow [48] \rightarrow [1] \\ \text{Grade 3 : } & [2] \rightarrow [48]_{\text{F}} \times 2 \rightarrow [48] \rightarrow [1] \\ \text{Grade 4 : } & [2] \rightarrow [48]_{\text{F}} \times 3 \rightarrow [48] \rightarrow [1]. \end{aligned} \quad (31)$$

$$\begin{aligned}
\text{Grade 1} &: [2] \rightarrow [128] \times 2 \rightarrow [1] \\
\text{Grade 2} &: [2] \rightarrow [128]_F \times 2 \rightarrow [128] \times 2 \rightarrow [1] \\
\text{Grade 3} &: [2] \rightarrow [128]_F \times 4 \rightarrow [128] \times 2 \rightarrow [1] \\
\text{Grade 4} &: [2] \rightarrow [128]_F \times 6 \rightarrow [128] \times 2 \rightarrow [1].
\end{aligned} \tag{32}$$

$$\begin{aligned}
\text{Grade 1} &: [2] \rightarrow [128] \times 3 \rightarrow [1] \\
\text{Grade 2} &: [2] \rightarrow [128]_F \times 3 \rightarrow [128] \times 3 \rightarrow [1] \\
\text{Grade 3} &: [2] \rightarrow [128]_F \times 6 \rightarrow [128] \times 3 \rightarrow [1] \\
\text{Grade 4} &: [2] \rightarrow [128]_F \times 9 \rightarrow [128] \times 3 \rightarrow [1].
\end{aligned} \tag{33}$$

Here, $[n]_F$ indicates a layer having n neurons with parameters, trained in the previous grades, remaining fixed during the training of the current grade.

For a multi-scale neural network [21] (MSDL), we consider the network with four subnetworks, each with the structure

$$[1] \rightarrow [8] \times 4 \rightarrow [1]$$

where the scale coefficients is $\{1, 2, 4, 8\}$.

Throughout the paper, ReLU is used as the activation function for SGDL, MSDL, and MGD.

E Supporting material for Sections 4-7

The experiments conducted in Sections 4-7 were performed on X86_64 server equipped with AMD 7543 @ 2.8GHz (64 slots) and AVX512, 2 x Nvidia Ampere A100 GPU.

The quality of the reconstructed image is evaluated by the peak signal-to-noise ratio (PSNR) defined by

$$\text{PSNR} := 10 \log_{10} \left((n \times 255^2) / \|\mathbf{v} - \hat{\mathbf{v}}\|_F^2 \right) \tag{34}$$

where \mathbf{v} is the ground truth image, $\hat{\mathbf{v}}$ is reconstructed image, n is the number of pixels in \mathbf{v} , and $\|\cdot\|_F$ denotes the Frobenius norm of a matrix.

E.1 Section 4

Supporting figures referenced in Section 4 include:

1. Figure 4: Clean images used in the paper.
2. Figures 5–6: Results for the ‘Image Regression’ in Section 4.
3. Figure 7: Noisy image used in the experiments. Figures 8–10: PSNR values during training and the denoised images produced by SGDL and MGD. These figures correspond to the ‘Image Denoising’ in Section 4.
4. Figure 11: Blurred image used in the experiments. Figures 12–14: PSNR values during training and the deblurred images produced by SGDL and MGD. These figures correspond to the ‘Image Deblurring’ in Section 4.

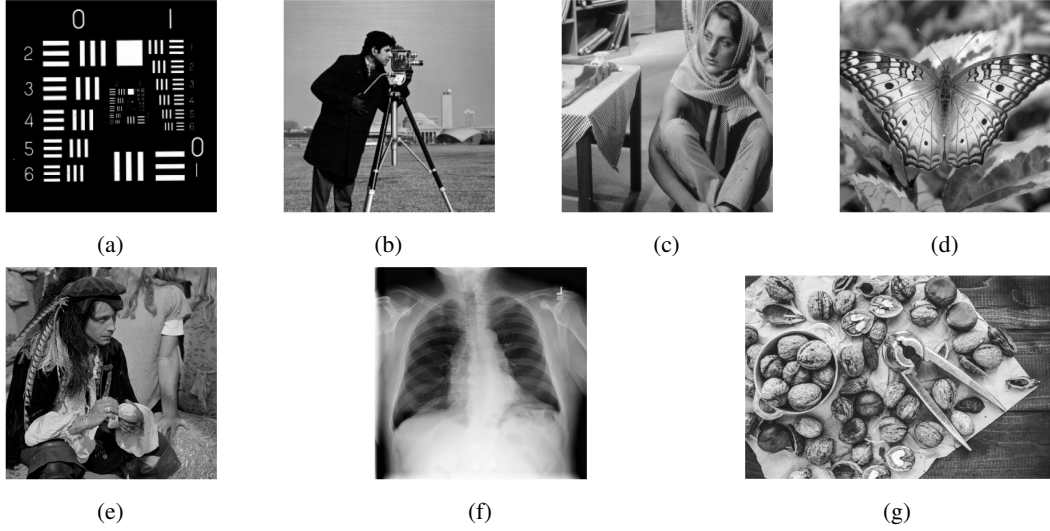


Figure 4: Clean images: (a) ‘Resolution chart’, (b) ‘Cameraman’, (c) ‘Barbara’, (d) ‘Butterfly’, (e) ‘Pirate’, (f) ‘Chest’, (g) ‘Walnut’.

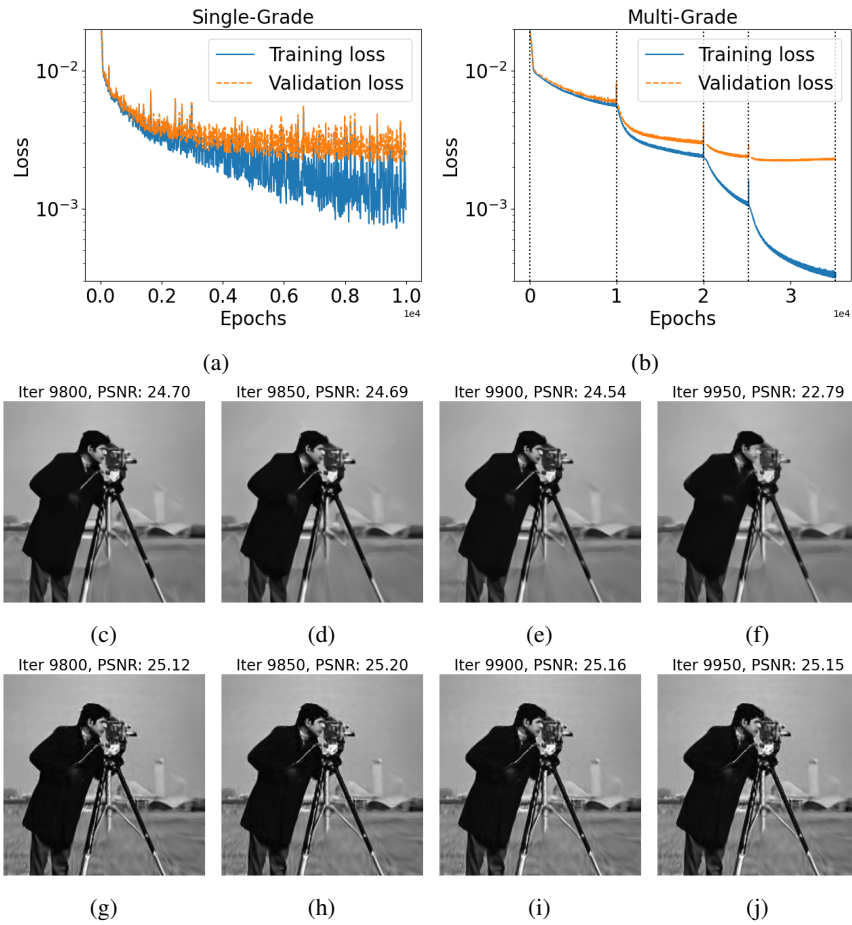


Figure 5: Comparison of SGDL and MGDL for the ‘Cameraman’ image. (a)-(b) show the loss curves for SGDL and MGDL. (c)-(f) present the SGDL predictions at iterations 9800, 9850, 9900, and 9950. (g)-(j) display the MGDL predictions at iterations 9800, 9850, 9900, and 9950 for grade 4. The PSNR values are provided in the titles of (c)-(j).

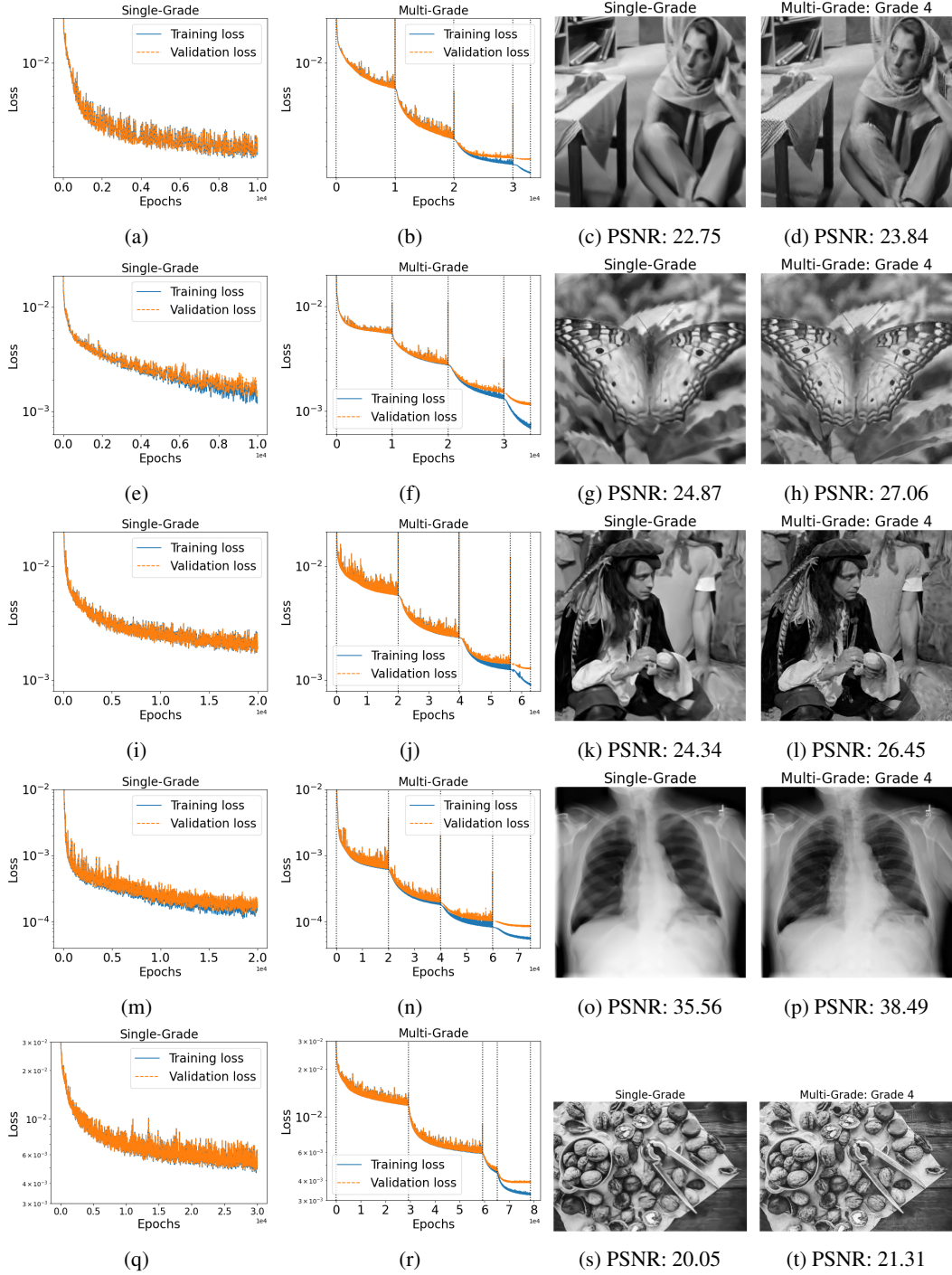


Figure 6: Comparison of SGDL and MGDL for image regression. (a)-(d): 'Barbara'; (e)-(h): 'Butterfly'; (i)-(l): 'Pirate'; (m)-(p): 'Chest'; (q)-(t): 'Walnut'.

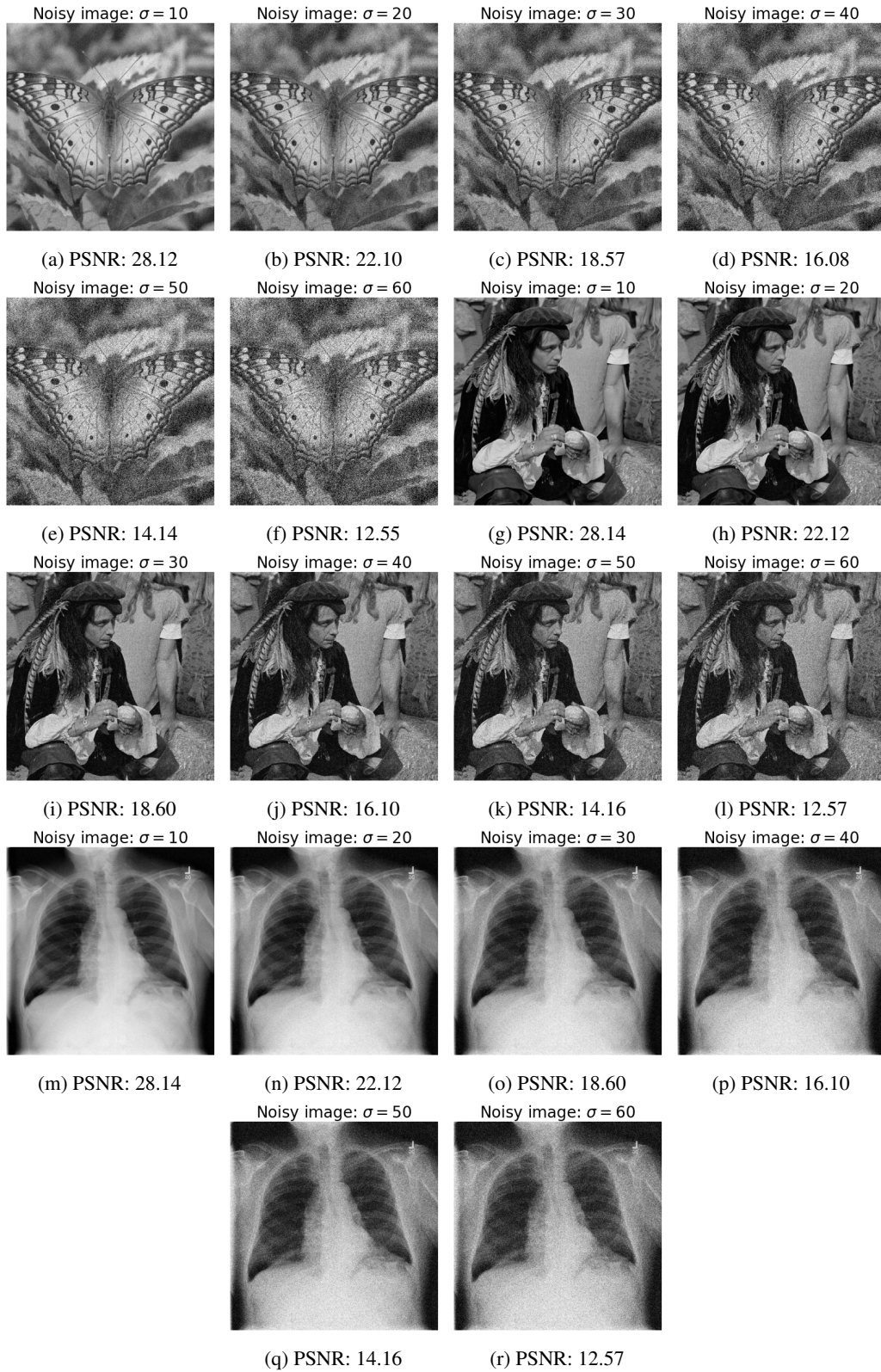


Figure 7: Noisy images: ‘Butterfly’ (a)-(f), ‘Pirate’ (g)-(l), and ‘Chest’ (m)-(r). The PSNR value is shown in each title.

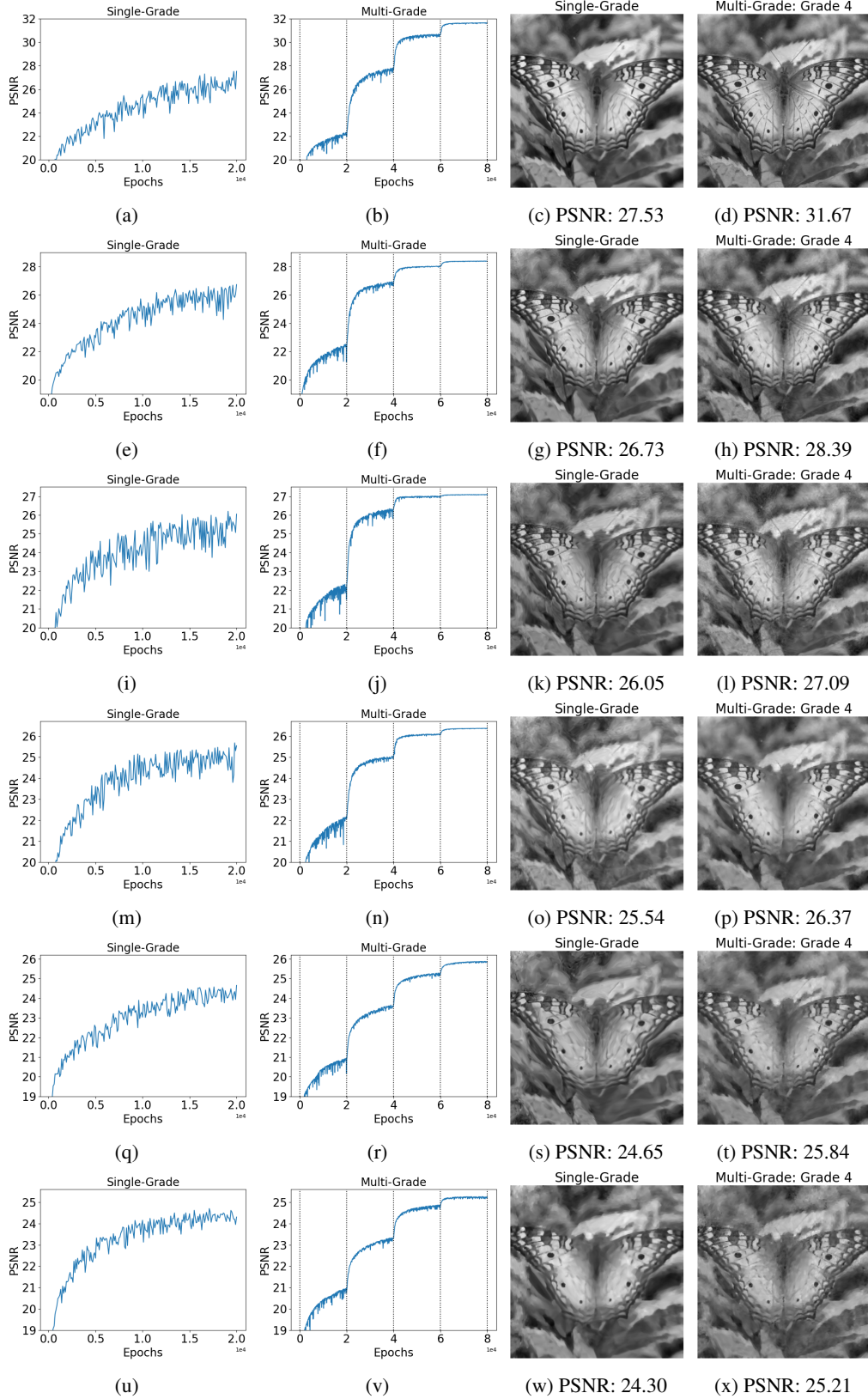


Figure 8: Comparison of SGDL (29) and MGDL (33) denoising results for the ‘Butterfly’ image. Rows one to six show noise levels $\sigma = 10, 20, 30, 40, 50, 60$, with PSNR during training and reconstructed images displayed with PSNR values in the subtitles.

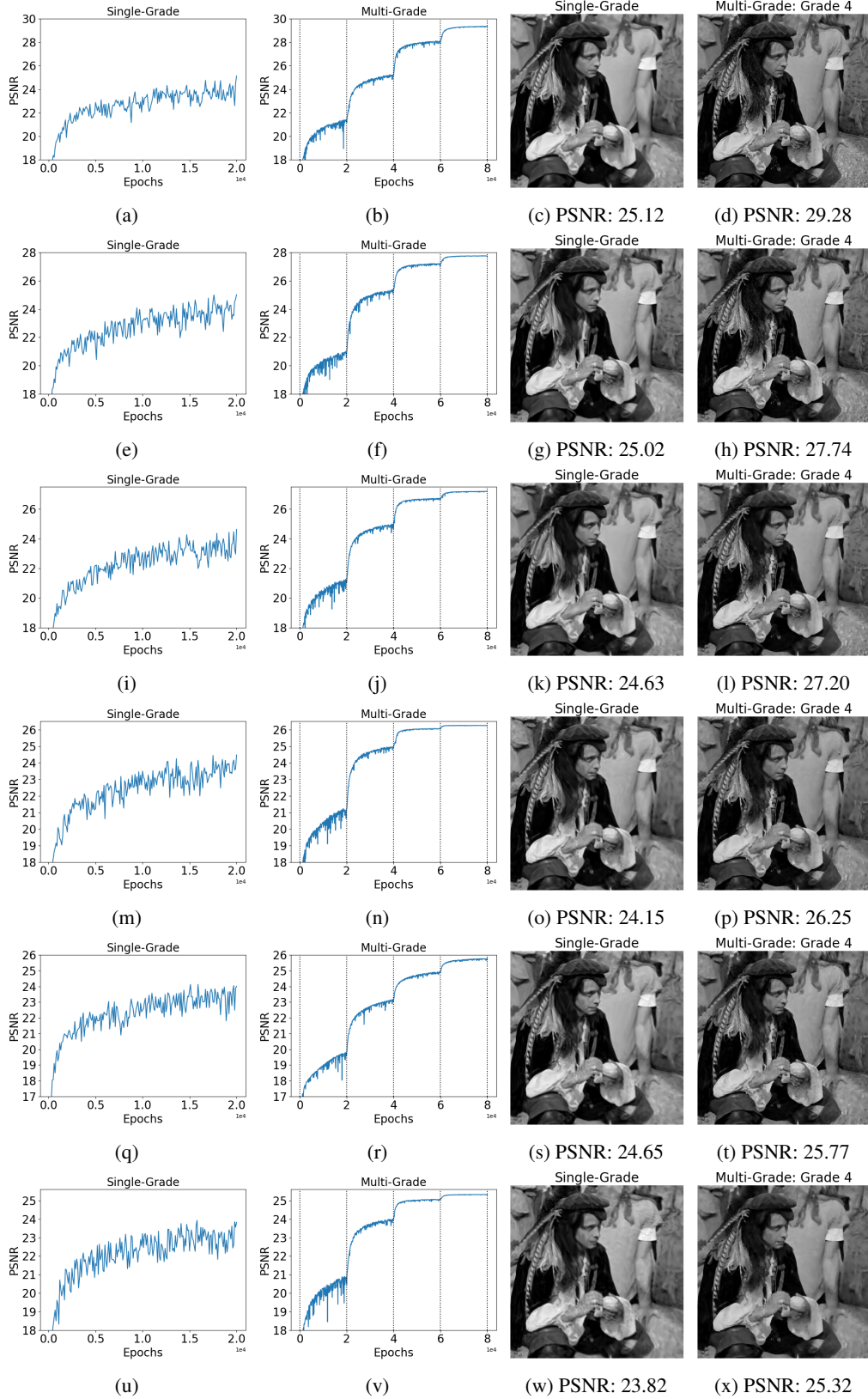


Figure 9: Comparison of SGDL (29) and MGDL (33) denoising results for the 'Butterfly' image. Rows one to six show noise levels $\sigma = 10, 20, 30, 40, 50, 60$, with PSNR during training and reconstructed images displayed with PSNR values in the subtitles.

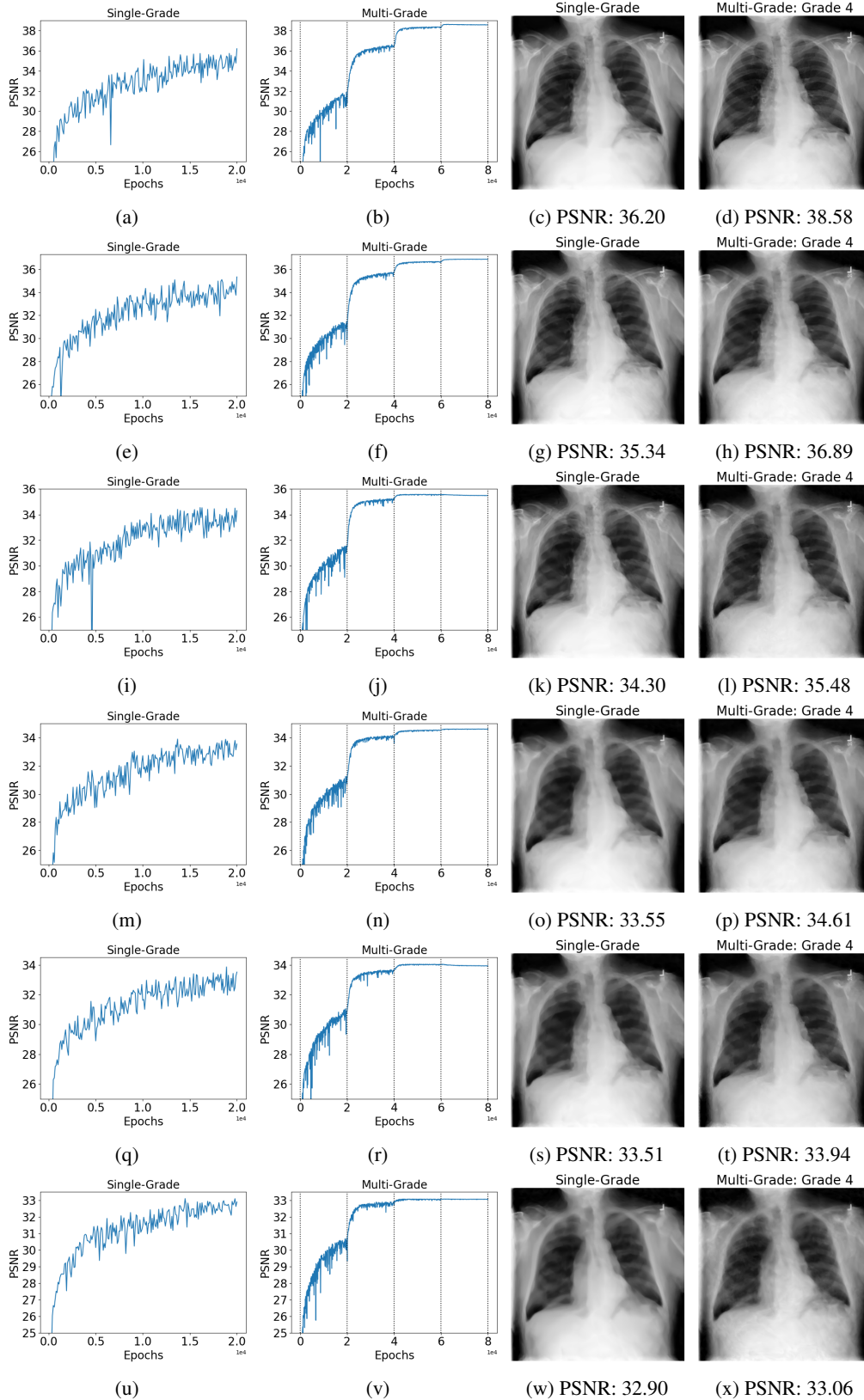


Figure 10: Comparison of SGDL (29) and MGD (33) denoising results for the ‘Chest’ image. Rows one to six show noise levels $\sigma = 10, 20, 30, 40, 50, 60$, with PSNR during training and reconstructed images displayed with PSNR values in the subtitles.

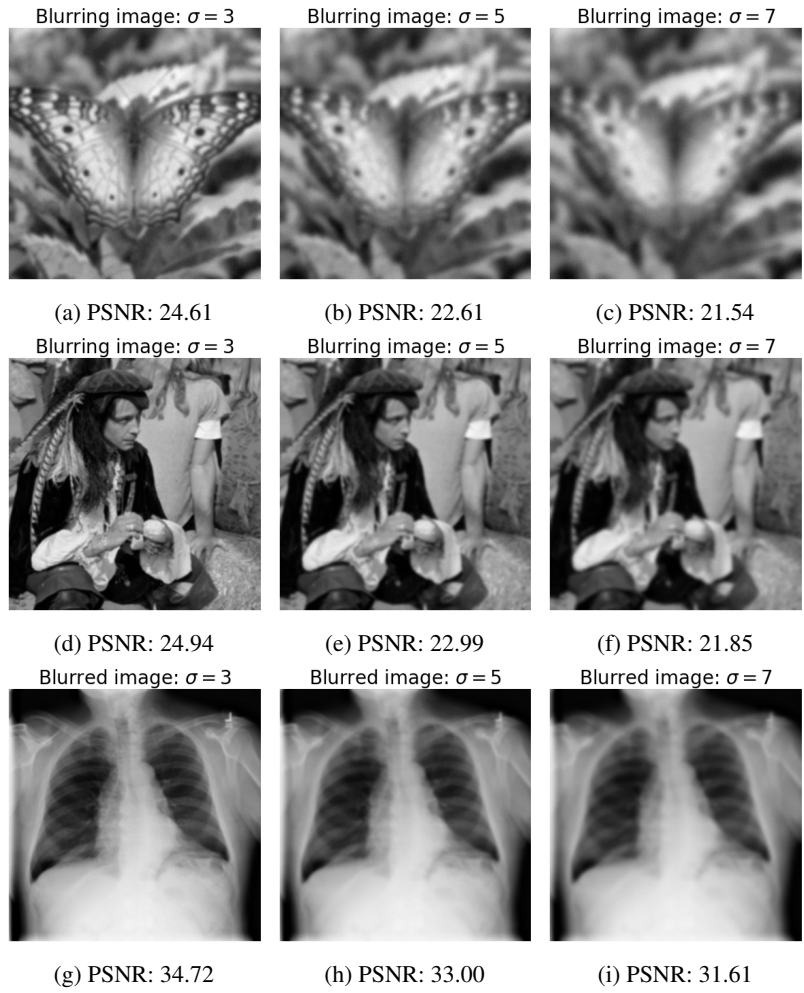


Figure 11: Blurred images: 'Butterfly' (a)-(c); 'Pirate' (d)-(f); 'Chest' (g)-(i). The PSNR value is shown in each title.

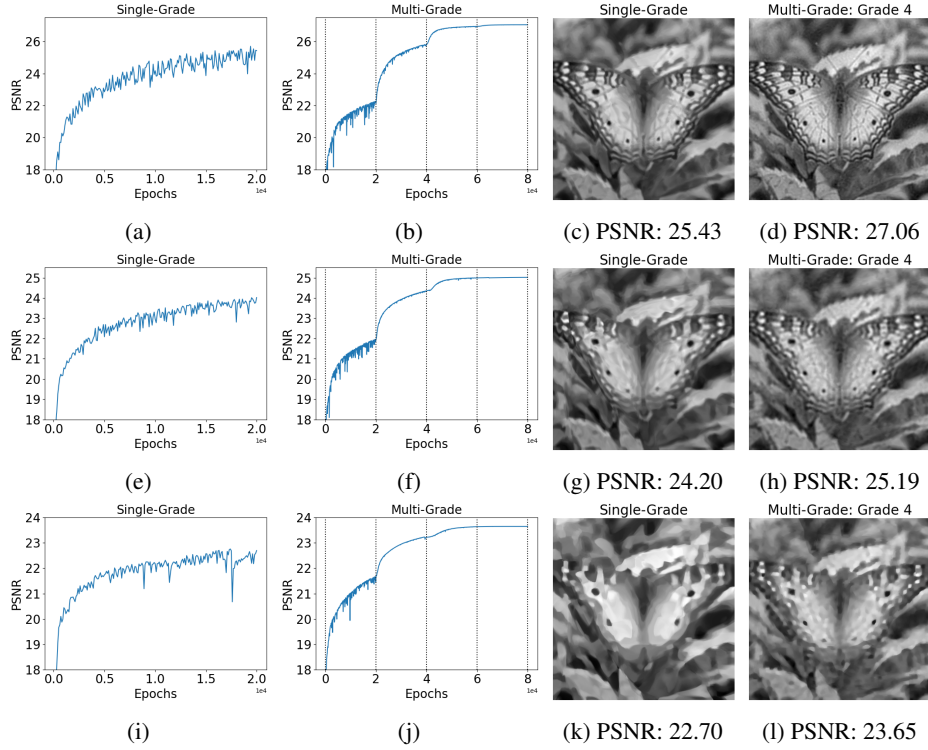


Figure 12: Comparison of SGDL (29) and MGDl (33) deburring results for the 'Butterfly' image. Rows one to three correspond to blurring kernel standard deviations $\hat{\sigma} = 3, 5, 7$.

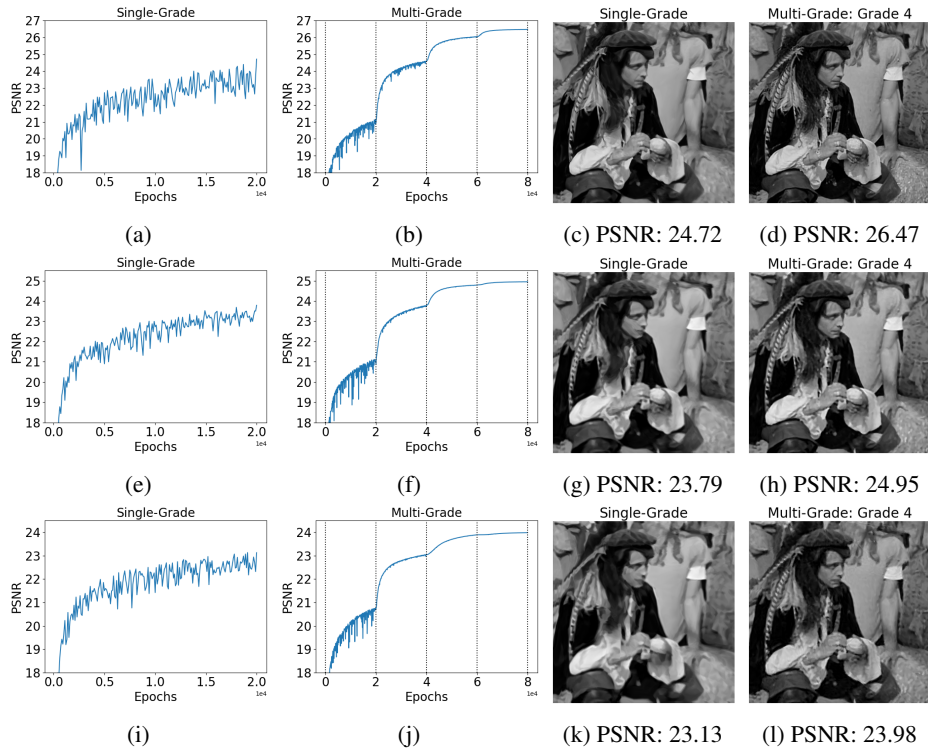


Figure 13: Comparison of SGDL (29) and MGDl (33) deburring results for the 'Pirate' image. Rows one to three correspond to blurring kernel standard deviations $\hat{\sigma} = 3, 5, 7$.

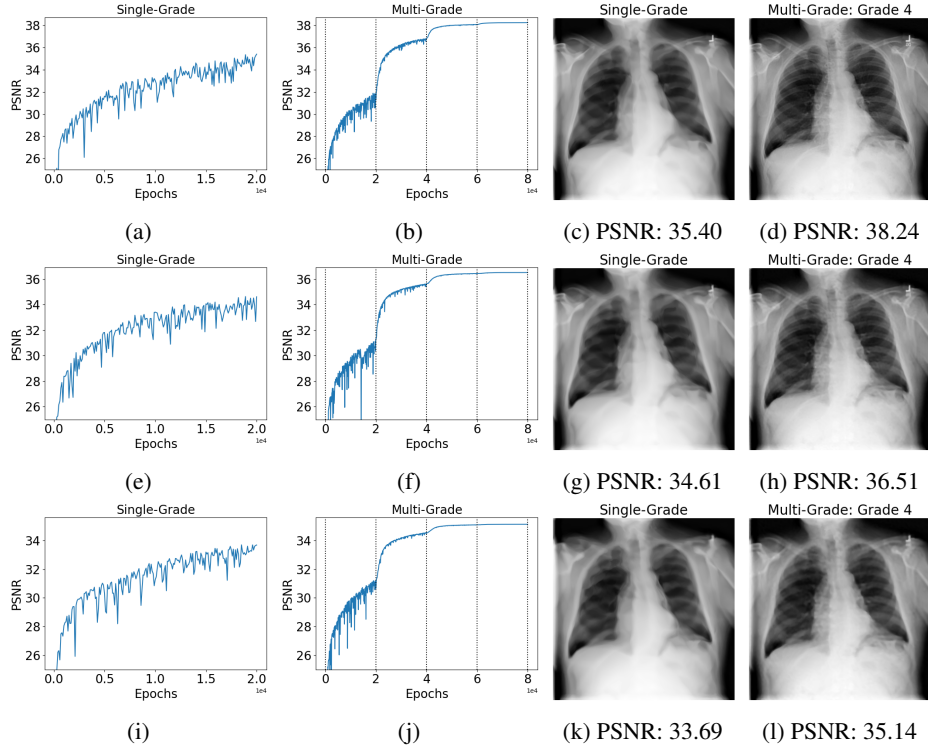


Figure 14: Comparison of SGDL (29) and MGDL (33) deburring results for the ‘Chest’ image. Rows one to three correspond to blurring kernel standard deviations $\hat{\sigma} = 3, 5, 7$.

E.2 Section 5

Figure 15 is the supporting figure referenced in Section 5, which presents the results for ‘Image Regression’.

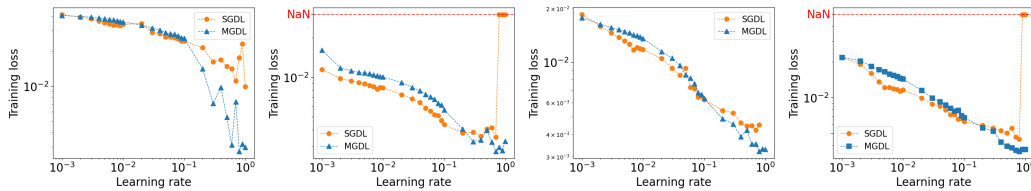


Figure 15: Impact of learning rate.

E.3 Section 6

The supporting figures referenced in Section 6 include:

1. Figures 16-17: Results for the ‘Synthetic data regression’ in Section 6.
2. Figures 18-20: Results for the ‘Image regression’ in Section 6.
3. Figures 21-24: Results for the ‘Image denoising’ in Section 6.

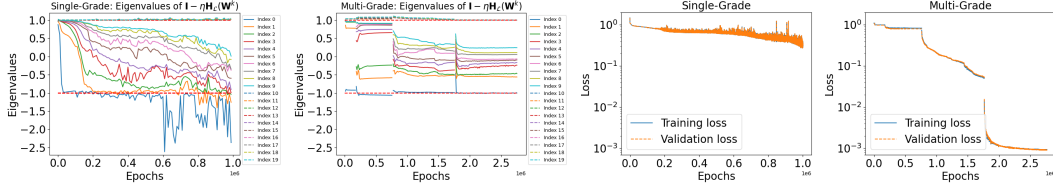


Figure 16: Training process of SGDL ($\eta = 0.005$) and MGDL (0.2) for Setting 2.

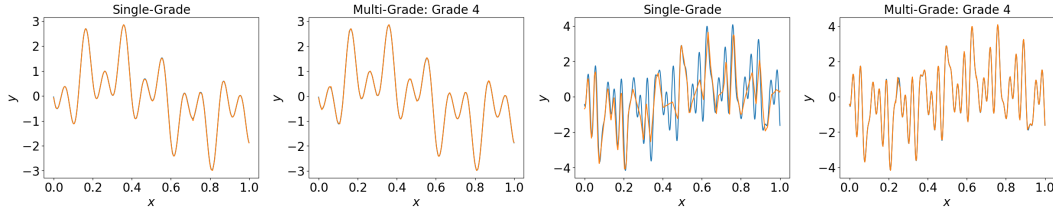


Figure 17: SGDL and MGDL predictions on synthetic data regression: Setting 1 (subfigures 1–2), Setting 2 (subfigures 3–4).

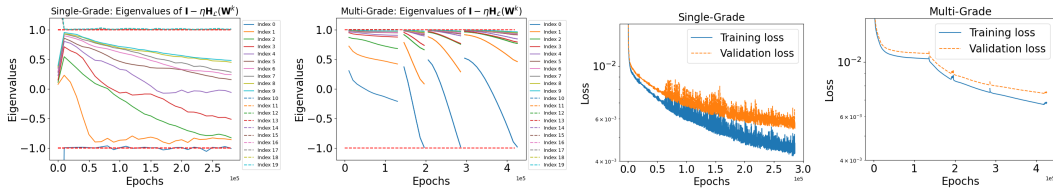


Figure 18: Training process of SGDL ($\eta = 0.1$) and MGDL ($\eta = 0.2$) for image ‘Cameraman’.

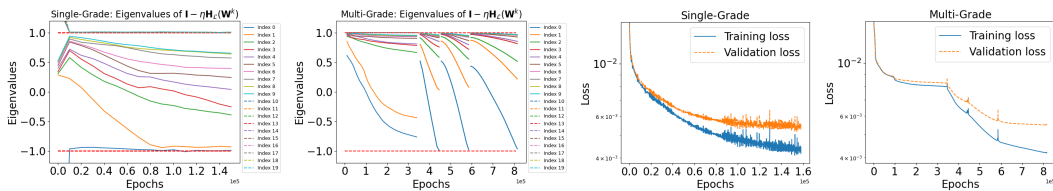


Figure 19: Training process of SGDL ($\eta = 0.08$) and MGDL ($\eta = 0.2$) for image ‘Barbara’.

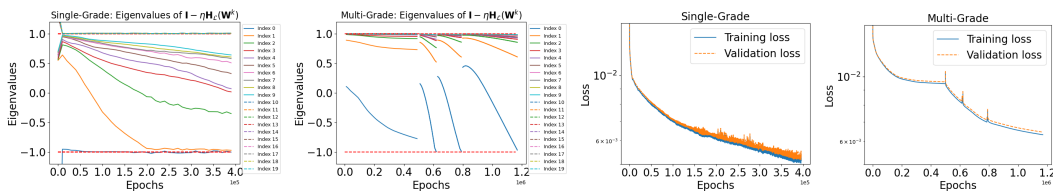


Figure 20: Training process of SGDL ($\eta = 0.05$) and MGDL ($\eta = 0.05$) for image ‘Butterfly’.

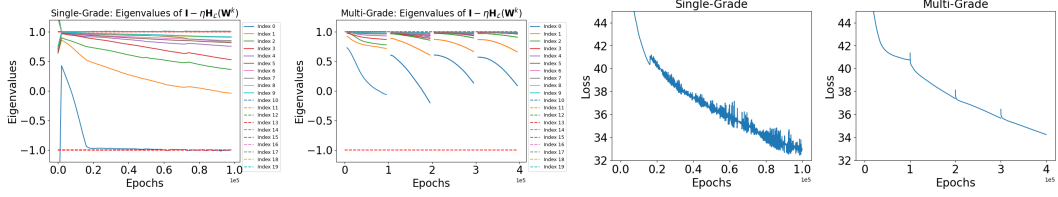


Figure 21: Training processes of SGDL and MGDL on the ‘Butterfly’ image (noise level 10).

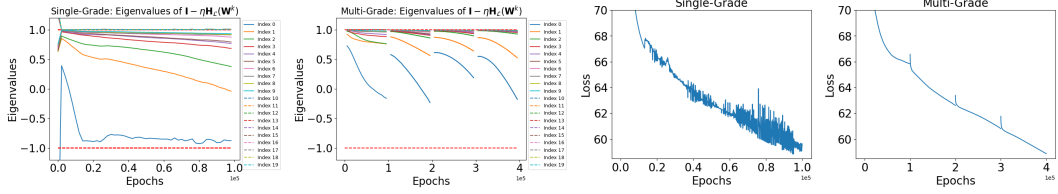


Figure 22: Training processes of SGDL and MGDL on the ‘Butterfly’ image (noise level 30).

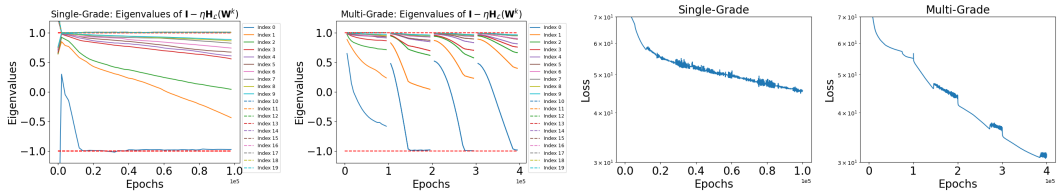


Figure 23: Training processes of SGDL and MGDL on the ‘Barbara’ image (noise level 10).

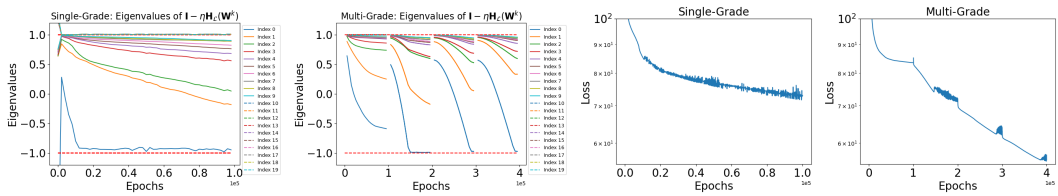


Figure 24: Training processes of SGDL and MGDL on the ‘Barbara’ image (noise level 30).

E.4 Section 7

The supporting Figures for Section 7 include Figures 25-28.

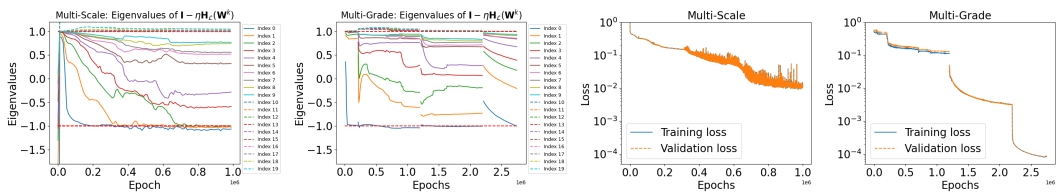


Figure 25: Training process of MSDL ($\eta = 0.004$) and MGDL ($\eta = 0.06$) for Setting 1.

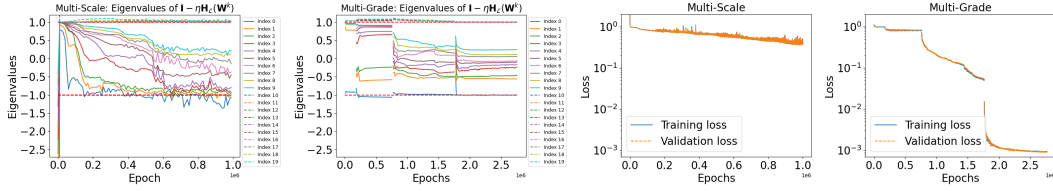


Figure 26: Training process of MSDL ($\eta = 0.006$) and MGD($\eta = 0.2$) for Setting 2.

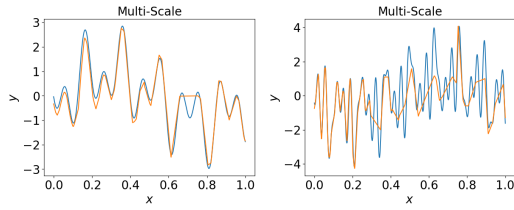


Figure 27: Prediction for MSDL.

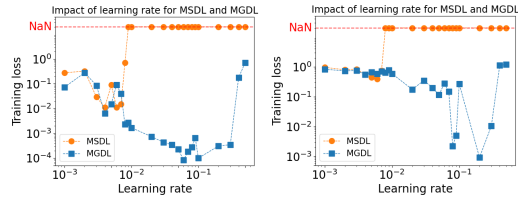


Figure 28: Impact of learning rate.